Coexistence and interplay of quantum and classical turbulence in superfluid ^{4}He: Decay, velocity decoupling, and counterflow energy spectra

S. Babuin,[1] V. S. L'vov,[2] A. Pomyalov,[2] L. Skrbek,[3] and E. Varga[3]
[1]*Institute of Physics ASCR, Na Slovance 2, 182 21 Prague, Czech Republic*
[2]*Department of Chemical Physics, The Weizmann Institute of Science, Rehovot 76100, Israel*
[3]*Faculty of Mathematics and Physics, Charles University, Ke Karlovu 3, 121 16 Prague, Czech Republic*
(Received 15 June 2016; revised manuscript received 25 September 2016; published 11 November 2016)

We report complementary experimental, numerical, and theoretical study of turbulent coflow, counterflow, and pure superflow of superfluid ^{4}He in a channel, resulting in a physically transparent and relatively simple model of decaying quantum turbulence that accounts for interactions of coexisting quantum and classical components of turbulent superfluid ^{4}He. We further offer an analytical theory of the energy spectra of steady-state quantum turbulence in the counterflow and pure superflow, based on algebraic approximation for the energy fluxes over scales. The resulting spectra are not of the classic Kolmogorov form, but strongly suppressed by the mutual friction, leading to the energy dissipation at all scales, enhanced by the counterflow-induced decoupling of the normal and superfluid velocity fluctuations.

DOI: 10.1103/PhysRevB.94.174504

I. INTRODUCTION

Flows of quantum fluids, such as ^{4}He below $T_\lambda \simeq 2.17$ K, displaying superfluidity and the two-fluid behavior, offer a challenging field of fundamental research combining quantum physics and fluid dynamics [1–3]. The phenomenological two-fluid model, suggested by Landau and Tisza, describes dynamics of superfluid ^{4}He in terms of interpenetrating normal and superfluid components that have their own densities $\rho_n(T)$, $\rho_s(T)$, and velocities $\boldsymbol{u}_n(\boldsymbol{r},t)$, $\boldsymbol{u}_s(\boldsymbol{r},t)$. In this paper, we consider finite temperature, above $\sim$1 K, where the normal component behaves as a classical fluid with the kinematic viscosity $\nu_n(T)$, while the superfluid component is inviscid, $\nu_s = 0$.

Due to the quantum mechanical restriction, the circulation around the superfluid vortices is quantized in integer values of $\kappa = h/m \simeq 10^{-3}\,\mathrm{cm}^2/\mathrm{s}$, where h is the Plank constant and m denotes the mass of ^{4}He atom. The singly quantized vortices usually arrange themselves in a tangle that can be characterized by vortex line density (VLD) $\mathcal{L}$, i.e., total length of the quantized vortex line in a unit volume. The dynamical behavior of the tangle constitutes an essential ingredient of *quantum turbulence*, the turbulence occurring in quantum fluids displaying superfluidity. The quantization of circulation in the superfluid component results in appearance of characteristic "quantum" length scale: the mean separation between vortex lines, $\ell = 1/\sqrt{\mathcal{L}}$, which is typically orders of magnitude smaller than the scale Δ of the largest (energy containing) eddies [4,5].

There is a growing consensus [3,6,7] that the quantization of vortex lines can be neglected at large scales $R \gg \ell$ and that quantum turbulence is similar to classical turbulence if excited similarly, for example, in a steady channel flow by a pressure drop [8–11] or when decaying behind a grid [12,13]. The reason is that the interaction of the normal-fluid component with the quantized vortex tangle leads to a mutual friction force [4,5,14] "which couples together $\boldsymbol{u}_n(\boldsymbol{r},t)$ and $\boldsymbol{u}_s(\boldsymbol{r},t)$ so strongly that they move as one fluid" [15]. On the other hand, at small length scales $R \lesssim \ell$, the quantization of vortex lines cannot be neglected and turbulence in superfluids has essentially quantum character.

The pipe and channel flows of viscous fluids belong to the class of most extensively studied classical flows [16,17]. As for pipe and channel flows of superfluids, by combining mechanical and thermal drive, a rich variety of two-fluid turbulent flows with different direction and flow ratio of the two components may be generated, representing a very complex superfluid hydrodynamics system [11,18,19] (see Fig. 1). The classical-like mechanical forcing (e.g., by compressing a bellows) results in a *coflow*, the closest analog to classical viscous channel flow, where both components move, on average, with the same velocity: the mean normal-fluid velocity $\boldsymbol{U}_n$ is equal to the mean superfluid velocity $\boldsymbol{U}_s$ (Fig. 1, right). However, due to quantum-mechanical constraints on the superflow, generated by individual lines, the velocity fields are completely different from the normal-fluid motions at scales $R \lesssim \ell$.

The normal and superfluid components of ^{4}He may also be made to flow relative to each other with a nonzero counterflow velocity $\boldsymbol{U}_{ns} \equiv \boldsymbol{U}_n - \boldsymbol{U}_s \neq 0$. The *thermal counterflow*, first systematically investigated in pioneering experiments by Vinen [20], is easily generated in a channel with one of its ends sealed and equipped with a heater and open at the other end to a superfluid helium bath (see Fig. 1, left). Here, both components move relative to the channel walls. The heat flux is carried away from the heater by the normal fluid alone, and, by conservation of mass, a superfluid current arises in the opposite direction: $\rho_n \boldsymbol{U}_n + \rho_s \boldsymbol{U}_s = 0$.

In this way, the counterflow velocity $\boldsymbol{U}_{ns}$, proportional to the applied heat flux, is created along the channel, soon accompanied by a tangle of vortex lines. In *pure superflow*, sketched in Fig. 1, middle, superleaks (i.e., filters located at the channel end with submicron-sized holes permeable only to the inviscid superfluid component) allow a net flow of the superfluid component in the channel: $\boldsymbol{U}_s \neq 0$, while the normal-fluid component is remaining, on average, at rest: $\boldsymbol{U}_n = 0$. In both cases, the fields $\boldsymbol{u}_s(\boldsymbol{r},t)$ and $\boldsymbol{u}_n(\boldsymbol{r},t)$ are expected to be different at all scales. Thermal counterflow and pure superflow therefore represent two special cases of counterflow, characterized by nonzero difference in mean flow velocities of the superfluid and normal components.

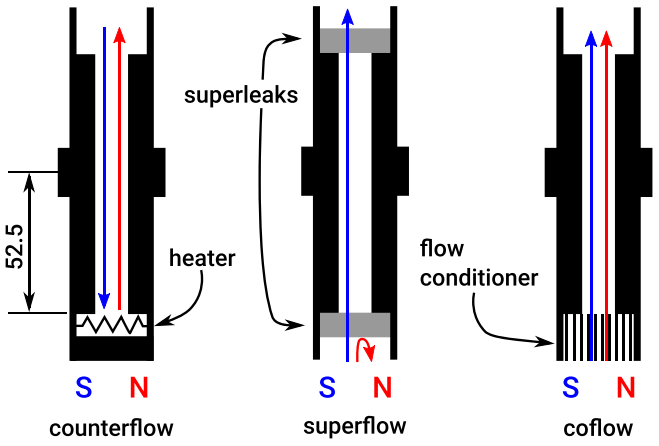

FIG. 1. Flow channels for the study of counterflow, pure superflow, and coflow. S and N stand for superfluid and normal components. Counterflow is produced thermally by a heater. Superflow and coflow are driven mechanically by a bellows. The turbulence is probed in the middle of the channel by second sound, excited and detected by mechanical vibration of a porous membrane.

In this paper, we report on complementary experimental, analytical, and numerical studies of the VLD decay $\mathcal{L}(t)$ of three categories of turbulent channel flows of superfluid ^{4}He, aiming to characterize the quantitative difference between the statistics of turbulence in the coflow on one hand, and the counterflow and superflow on the other. Our study is based on detailed analysis of the VLD decay from three different initial values of $\mathcal{L}_0 \sim 10^4$, 10^5, and 10^6 cm^{-2}, in all three types of the flows, obtained at different temperatures in the same channel. Although part of them was previously published [9,21], the whole set of data was never presented simultaneously, thus covering the large span of experimental parameters in a systematic manner, which allows their meaningful theoretical analysis. Our results represent substantial extension of a recent paper by Gao *et al.* [22], which considered only decaying counterflow. The experimental technique is shortly reviewed in Sec. II A and sketched in Fig. 1.

In Figs. 2 and 3, we present the typical experimental time dependencies of $\mathcal{L}(t)$ decaying by two–three orders of magnitude and analyze them in Sec. II B. We demonstrate that the initial stage of decay in all three types of the flow, including the coflow regime, typically follows a form

$$\mathcal{L}(t) \Rightarrow \mathcal{L}^{\mathrm{Q}}(t) = \frac{b_1 \mathcal{L}_0 |\tau_1|}{t - \tau_1}, \quad \mathcal{L}_0 \equiv \mathcal{L}(t=0), \tag{1a}$$

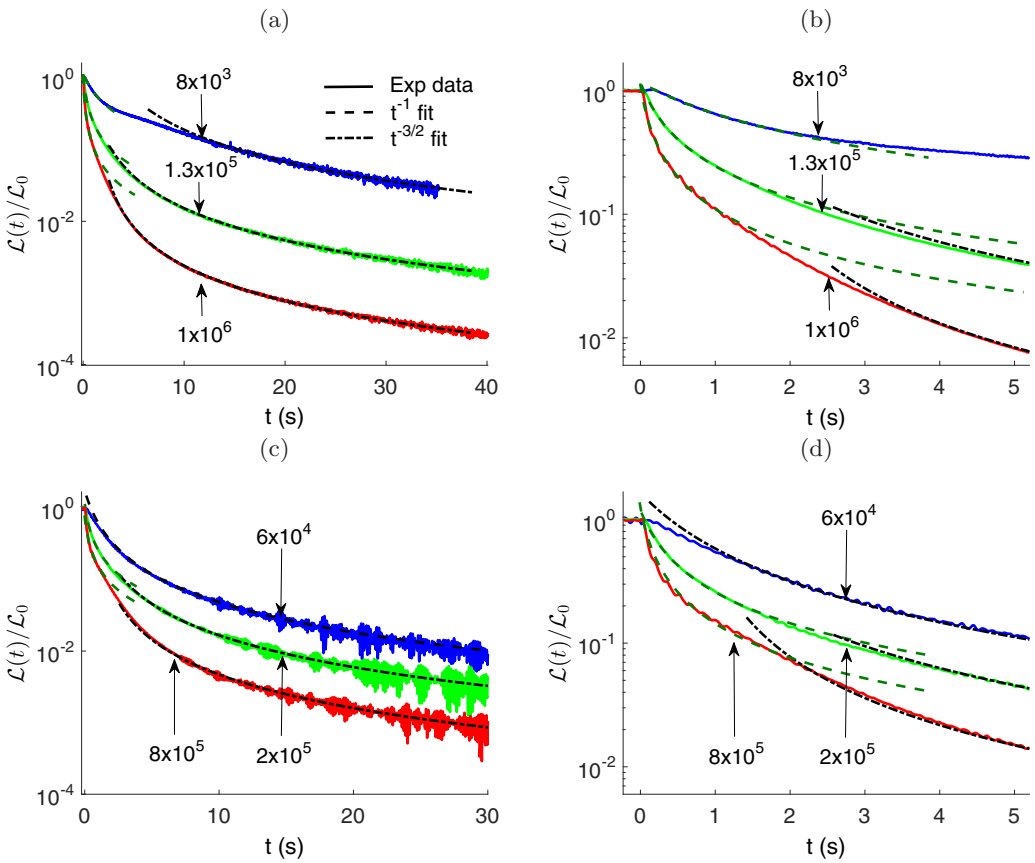

FIG. 2. Experimental data of the VLD decay $\mathcal{L}(t)/\mathcal{L}_0$ in the coflow (in the 7-mm channel), normalized by initial VLD $\mathcal{L}_0$. The lines correspond (from top to bottom) for $\mathcal{L}_0 \simeq 10^4$ (blue lines), 10^5 (green lines), and 10^6 (red lines). The explicit values of $\mathcal{L}_0$ are shown in figures. Data for $T = 1.35$ K are shown in panels (a) and (b), and for $T = 1.45$ K in panels (c) and (d). The panels (b) and (d) emphasize the details of the short-time behavior. Quantum t^{-1} fits [Eq. (1a)] are shown by dashed dark green lines, while the classical $t^{-3/2}$ fits [Eq. (1b)] by black dotted-dashed lines.

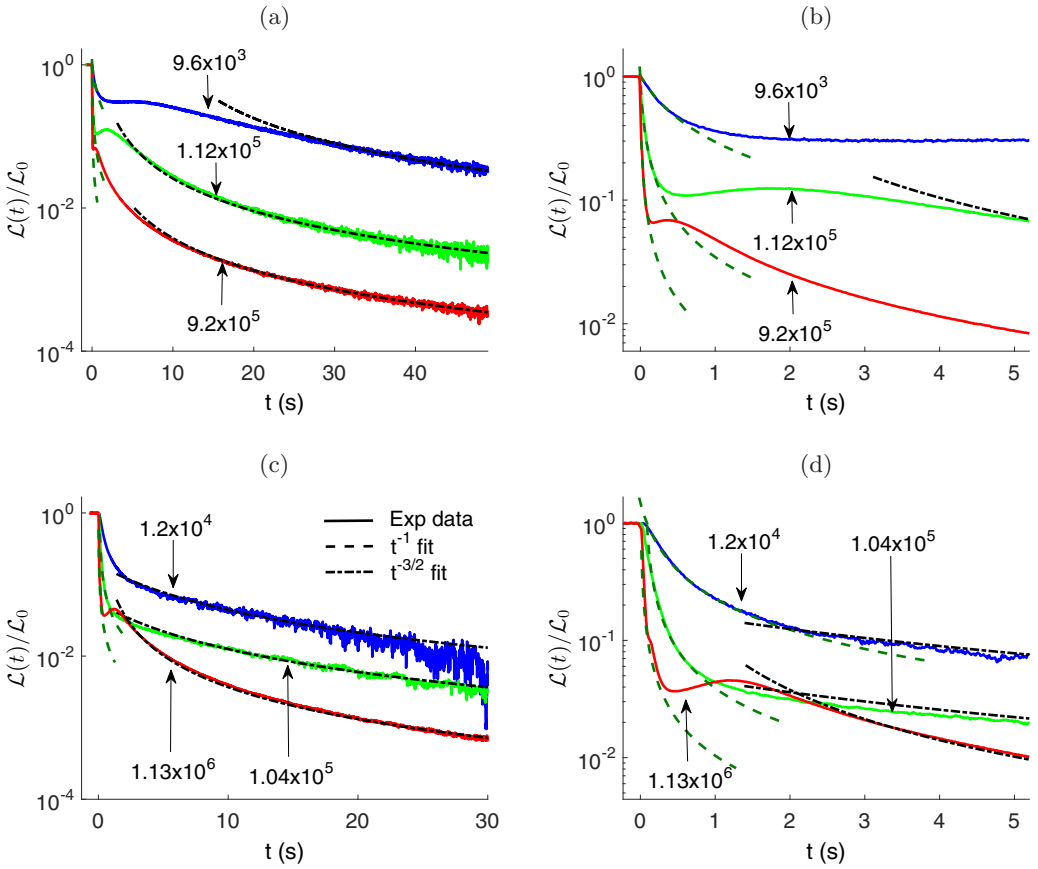

FIG. 3. Experimental data for the VLD decay $\mathcal{L}(t)/\mathcal{L}_0$ at $T = 1.45$ K, normalized by initial VLD $\mathcal{L}_0$. The results for counterflow are shown in (a) and (b), for superflow in (c) and (d). In all panels, the lines correspond to (from top to bottom) $\mathcal{L}_0 \simeq 10^4$ (blue lines), 10^5 (green lines), and 10^6 (red lines). The explicit values of $\mathcal{L}_0$ are shown in the figure. As in Fig. 2, quantum t^{-1} fits [Eq. (1a)] are shown by dashed dark green lines, while the classical $t^{-3/2}$ fits [Eq. (1b)] by black dotted-dashed lines. The panels (b) and (d) show the initial stages of the decay.

with two fitting parameters: the virtual origin time τ_1 and the dimensionless parameter b_1. The asymptotics (1a) may be rationalized in the framework of the Vinen equation for $\mathcal{L}(t)$ [20] as the decay of random tangle of quantized vortex lines. The energy spectrum of this vortex tangle in the superfluid component (the energy distribution between scales, presented in the k space) $\mathcal{E}_s^Q(k)$ is dominated by the intervortex scales $\ell k \sim 1$.

The late stage of the decay, discussed in Sec. II B, follows a $t^{-3/2}$ asymptotics [13] and may be described by

$$\mathcal{L}(t) \Rightarrow \mathcal{L}^{cl}(t) = \frac{b_2 \mathcal{L}_0 |\tau_2|^{3/2}}{(t-\tau_2)^{3/2}}, \tag{1b}$$

with two new fitting parameters: τ_2 and b_2. It is commonly believed that the dependence (1b) is caused by the classical Richardson-Kolmogorov cascade in the superfluid component, with $\mathcal{E}_s^{cl}(k) \propto k^{-5/3}$ spectrum. The parameters of the flows, chosen for the analysis and the fitting parameters, are summarized in Table I.

A natural way to rationalize these observations is to assume that the turbulent energy spectrum of the superfluid component $\mathcal{E}_s(k)$ consists of two parts:

$$\mathcal{E}_s(k) = \mathcal{E}_s^Q(k) + \mathcal{E}_s^{cl}(k), \tag{2}$$

(i) the classical region spanning large scales from the integral length scale Δ down to the intervortex distance ℓ, where it is followed by (ii) a quantum contribution $\mathcal{E}_s^Q(k)$, corresponding to the random tangle of quantized vortex lines, having a form of a peak. Qualitatively, it is sketched in Fig. 4 and explained in more details in Sec. II C.

Section III is devoted to phenomenological modeling of the entire set of experimental data, in a unified manner, which stems from understanding of the underlying spectral properties of the studied flows. The previous analytical results [22] required by the model are shortly reminded for self-sufficiency of the presentation.

First of all, based on explained above forms of the energy spectra for coflow, Fig. 4(a), we suggest in Sec. III A a "basic model" of the VLD decay [Eq. (17)], in which the quantum decay term (9a) and the classical energy source term (16) are present from the very beginning of the decay, $t = 0$. This model reproduces both quantum and classical asymptotics, given by Eqs. (1), in agreement with the observations in coflow, shown in Figs. 2 and 3. Based on the basic model, in Sec. III B we present a more detailed (but still preliminary) discussion of the underlying physics, hidden in its fitting parameters. Although the model explains small- and large-time asymptotics of the $\mathcal{L}(t)$ dependence, it fails to describe the crossover regime between them, even for the coflow.

TABLE I. Column #2 shows types of the flow and channel width of chosen 12 sets of experiments, numbered in first column from 1 to 12). Next 17 columns display: #3, temperature T in K; #4, #5, and #6, superfluid, normal fluid, and counterflow velocities U_s, U_n, and U_{ns} in cm/s; #7, initial VLD $\mathcal{L}_0$ in cm^{-2}; #8, Reynolds number Re_τ, estimated via counterflow velocity U_{ns} and normal-fluid kinematic viscosity ν_n; #8–#12: parameters of the fits (1a) for the Vinen's ($\propto t^{-1}$) decay and for the hydrodynamic ($\propto t^{-3/2}$) decay(1b), namely #9 and #11, dimensionless b_1 and b_2 and #10 and # 12, time origins τ_1 and τ_2 in seconds; #13, ratio of the initial VLD $\mathcal{L}_0$ to $\mathcal{L}_1$, lowest value of $\mathcal{L}(t)$ in the t^{-1} fit at the time $t = t_1$ (shown in #15); #14, ratio of the VLD $\mathcal{L}_1$ to $\mathcal{L}_2$, the initial (largest) value of $\mathcal{L}(t)$ in the $t^{-3/2}$ fit at the time $t = t_2$ (shown in #16); #17 and #18, model parameters d_1 and d_2, related to b_1 and b_2 by Eqs. (10) and (18b) (with $\alpha = 0.06$ for $T = 1.45$ K and $\alpha = 0.04$ for $T = 1.35$ K); #19, ratio of the initial VLD $\mathcal{L}_0$ to $\mathcal{L}_2$.

1	2	3	4	5	6	7	8	9	10	11	12	13	14	15	16	17	18	19
#	Type of the flow	T (K)	U_s (cm/s)	U_n (cm/s)	U_{ns} (cm/s)	$\mathcal{L}_0 \times 10^{-4}$ (cm^{-2})	Re_τ	b_1	τ_1 (s)	b_2	τ_2 (s)	$\mathcal{L}_0/\mathcal{L}_1$	$\mathcal{L}_1/\mathcal{L}_2$	t_1 (s)	t_2 (s)	d_1	d_2	$\mathcal{L}_0/\mathcal{L}_2$
1			0.69	0.69	0	0.86	139	−1.27	−1.26	−2.22	−0.08	2.3	3.9	2.0	14	0.54	−0.0035	8.97
2		1.35	4.99	4.99	0	13.3	797	−1.19	−0.26	−0.22	−0.05	5.9	4.3	1.4	5.3	1.73	−0.019	25.4
3	Co-		22.4	22.4	0	106	3092	−1.15	−0.11	−0.001	1.15	12.5	4.7	1.3	3.6	5.36	0.0049	58.8
4	flow,				0	6.0	843	−1.04	−0.8	−0.03	−1.0				1.7	3.05	−0.0092	4.16
5	7 mm	1.45	4.99	4.99	0	20.0	3276	−1.09	−0.28	−0.05	−0.2	5.6	3.6	1.6	4.5	3.70	−0.0039	20.2
6			22.4	22.4	0	80.0		−1.25	−0.13	0.006	0.5	7.7	13	1.2	5.0	7.92	0.0046	100
7	Counter-		−0.09	0.95	1.05	0.96	0.96	−1.02	−0.41	0.03	6.0	2.0	7.0	1.5	2.7	0.24	0.0547	14.0
8	flow,	1.45	−0.29	2.89	3.18	11.2	775	−0.90	−0.04	0.18	0.1	6.3	2.9	0.7	8.1	0.25	0.0070	18.3
9	10 mm		−0.77	7.77	8.54	92.5	1888	−0.61	−0.013	−0.25	−0.01	13.2	38	0.1	3.1	0.45	−0.0019	502
10	Super-		0.96	0	0.96	1.21	176	−1.40	−0.18	−0.01	−7	6.3	2.9	0.4	32	0.18	−0.0340	18.3
11	flow,	1.45	2.67	0	2,67	10.4	467	0.49	0.07	−0.003	−5.8	17.2	3.9	0.2	6.0	0.22	−0.0516	67.1
12	10 mm		7.41	0	7.41	113	1246	0.25	0.04	−0.015	−0.15	9.1	5.5	0.1	12	0.68	−0.0065	50.1

The most striking disagreement between the simple "basic" model and observations, seen in Fig. 3, is a "bump" (nonmonotonic behavior) in the $\mathcal{L}(t)$ dependence, in the counterflow and superflow cases. This behavior may be explained by the delay in the delivery of the energy flux from the classical to the quantum part of the spectra suggested in the recent paper by Gao *et al.* [22] for the special case of decaying thermal counterflow required for the evolution from a more localized in k spectrum, sketched in Fig. 4(b), toward the K41 spectrum, shown in Figs. 4(a) and 4(c).

An essential part of our further analysis is based on the reported in Sec. III C results of the numerical simulations of the energy spectra evolution, that allowed to clarify the details of the energy-flux delay in the decaying counterflow turbulence.

This delay is accounted for in the "improved model" of the VLD decay, formulated in Sec. III D. In this section, we suggest an analytical expression of the $\mathcal{L}(t)$ dependence, that agrees with the main experimental observations in the *entire* duration of the decay: the known short-time $\propto 1/t$ and long time $\propto 1/t^{3/2}$ asymptotes as well as the bump in the $\mathcal{L}(t)$ dependence at the crossover times.

Following analysis of our experimental findings, we develop in Sec. IV an analytical theory of the steady-state quantum turbulence in the counterflow and pure superflow, that results in prediction of the energy spectra and velocity structure functions in a reasonable agreement with known experimental results. Our theory is based on the algebraic approximation for the energy fluxes over scales. The resulting spectra are strongly

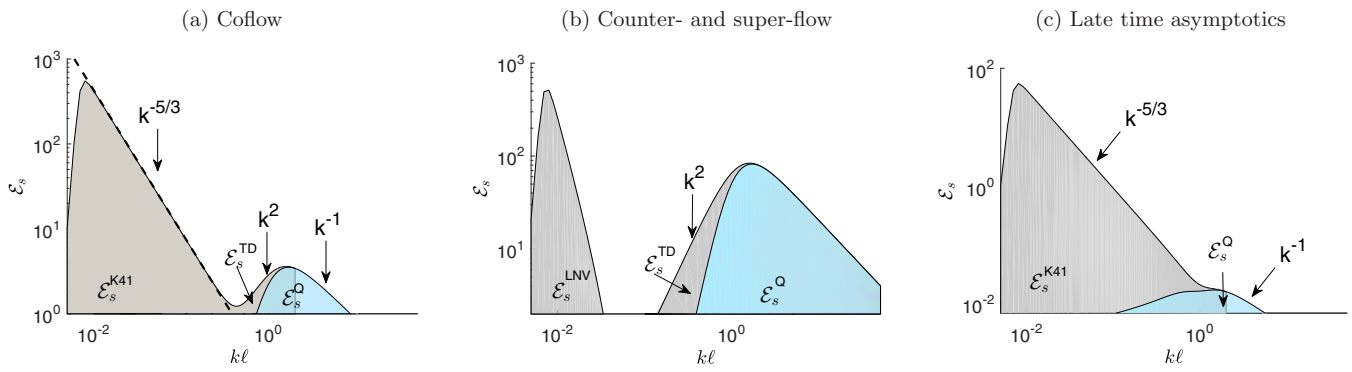

FIG. 4. Sketch of the stationary superfluid turbulent energy spectrum in log-log coordinates $\log \mathcal{E}_s(k)$ vs $\log(k\ell)$. According to Eq. (2), the spectrum $\mathcal{E}_s(k)$ consists of a classical $\mathcal{E}_s^{cl}(k)$ and a quantum $\mathcal{E}_s^{Q}(k)$ part, colored in light blue and cyan, respectively. In the coflow (a), $\mathcal{E}_s^{cl}(k)$ consists of a cascade part $\mathcal{E}_s^{K41}(k) \propto k^{-5/3}$ (for $k < k_\times$, $k_\times = \rho\Omega/\rho_n$) and a thermodynamic equilibrium part $\mathcal{E}_s^{TD}(k) \propto k^2$ for $1/\ell \gtrsim k > k_\times$. In the counterflow and pure superflow (b), the quantum contribution $\mathcal{E}_s^{Q}(k)$ and the classical thermal bath part $\mathcal{E}_s^{TD}(k)$ look similar to that in coflow, while the cascade part, the supercritical LNV spectrum $\mathcal{E}_{sp}$ [Eqs. (7)] terminates at some $k_* < 1/\ell$ and does not provide energy to the quantum vortex tangle in the stationary regime. After switching off the counterflow or pure superflow, the spectrum shown in (b) evolves to that shown in (c), switching on the energy flux toward quantum vortex tangle after some delay.

suppressed by the mutual friction, leading to the energy dissipation at all scales, enhanced by the counterflow-induced decoupling of the normal and superfluid velocity fluctuations.

In the final Sec. V we summarize our main results and discuss the issues that remain out of the scope of this research. In particular, we stress that our simple analytical theory of the steady-state energy spectra of quantum turbulence in the counterflow adopts some uncontrolled approximations and simplifications, widely used in the studies of classical hydrodynamic turbulence. In the further studies of quantum turbulence, these assumptions have to be either better justified or relaxed. Nevertheless, we consider our findings as a natural and perhaps even required step in this direction.

II. DECAY OF THE VORTEX TANGLE IN COFLOW, COUNTERFLOW, AND SUPERFLOW

A. Experiment

The superflow and the coflow of superfluid ^{4}He are both mechanically forced by a low temperature bellows through a square cross-section brass channel, illustrated in Fig. 1. The same channel can be configured to attain superflow, coflow, and thermal counterflow. For superflow, sintered silver filters (superleaks) block the viscous normal component. Two vertical brass flow channels have been used, both with the test section 105 mm in length and has an internal square cross section of side 7 and 10 mm, therefore with a factor 2 change in cross-sectional area. For coflow, the superleaks are removed and the lower one is replaced by a flow conditioner made from a dense pack of 10-mm-long capillaries of 1 mm diameter, intended to cut larger-scale turbulent eddies. The counterflow is prepared by closing one end of the channel with a resistive wire heater and leaving the other end open. A full description of the mechanically driven superflow apparatus and the measurement technique is given in Ref. [23]. Counterflow is studied as in previous Prague experiments [24,25].

Turbulence is detected by measuring the extra attenuation of second sound caused by the scattering of normal-component thermal excitations by the vortex lines. Second sound is generated and detected by a pair of vibrating porous membranes located in the walls of the channel at its midpoint; the sound travels across the channel, which acts as a resonator. The time-dependent attenuated amplitude of second sound at resonance $a(t)$ can be related to the instantaneous VLD $\mathcal{L}(t)$ (assuming random and not extremely dense tangle [23]) through the equation $\mathcal{L}(t) = \frac{6\pi\Delta f_0}{B\kappa}[\frac{a_0}{a(t)} - 1]$, where a_0 and Δf_0 are the amplitude and full width at half maximum of the second-sound amplitude resonant curve for quiescent helium, and B is the mutual friction coefficient of order unity, tabulated in Ref. [26]. The attenuation of second sound measures the length of vortex line per unit volume weighted by a factor $\sin^2\theta$, where θ is the angle between any element of vortex line and the direction of propagation of the second sound.

We have performed mechanically driven coflow, superflow, and thermally driven counterflow decay measurements, in the two channels of widths $2\Delta = 7$ and 10 mm, in the temperature range between 1.25 to 2.10 K, and for different values of velocities chosen such to produce initial steady-state VLD $\mathcal{L}_0$, spaced almost exactly one decade apart: 10^4, 10^5, and 10^6 cm^{-2}. For every combination of temperature and starting line density we have measured typically 150 individual decays, under nominally identical experimental conditions and we have ensemble averaged these samples, allowing us to resolve up to four orders of magnitude of decay on $\mathcal{L}(t)$.

B. Experimental data and their preliminary analysis

In this paper, we restrict ourselves by discussing 12 typical data sets of experiments, characterized in Table I, which are chosen to illustrate the basic ideas of this research. For $T = 1.45$ K we discuss three sets with $\mathcal{L}_0 \sim 10^4$, 10^5, and 10^6 cm^{-2} for coflow (sets #3, #4, and #5), counterflow (sets #7, #8, and #9) and superflow (sets #10, #11, and #12). In addition, we analyze the coflow sets for lower $T = 1.35$ K with the same $\mathcal{L}_0 \sim 10^4$, 10^5, and 10^6 cm^{-2} (sets #1, #2, and #3).

The experiments were conducted in the channels of two different widths. For coflow, we have more representative experimental data with 7-mm channel, while for superflow and counterflow more representative data were obtained with 10-mm channel. We found no significant differences between 7- and 10-mm-channel results for a given flow type and therefore compare below the most representative results regardless of the channel width.

1. Coflow

We begin to analyze the time evolution of $\mathcal{L}(t)$ from the decaying coflow turbulence, which, in some sense, is the simplest case. The VLD $\mathcal{L}(t)$ is decaying monotonically, as illustrated in Fig. 2 for both temperatures $T = 1.35$ K [shown in Figs. 2(a) and 2(b)] and $T = 1.45$ K [shown in Figs. 2(c) and 2(d)] and for all three initial values of $\mathcal{L}_0$: 10^4 cm^{-2} (blue lines), 10^5 cm^{-2} (green lines), and 10^6 cm^{-2} (red lines). There is no qualitative difference between two presented temperatures, except that for higher $T = 1.45$ K the VLD $\mathcal{L}(t)$ is decaying slightly faster. Thus, there is no reason to analyze these cases separately.

Our first step is an analysis of the initial stage of the coflow turbulence decay shown in Figs. 2(b) and 2(d) (for $T = 1.35$ and 1.45 K) fitted by t^{-1} law (1a), as shown by dashed lines. The fitting parameters b_1 and τ_1, given in Table I, will be discussed later. For now, we notice that the negative virtual origin time τ_1 increases (and becomes closer to zero) with increasing $\mathcal{L}_0$, as expected from Eq. (1a).

As seen in Figs. 2(b) and 2(d), the "quantum" t^{-1} fit (1a) agrees with the experimental data over the time interval $0 \lesssim t \lesssim t_1$ about 1–2 s, when $\mathcal{L}(t)$ decays from $\mathcal{L}_0$ to $\mathcal{L}(t_1) \equiv \mathcal{L}_1$. Ratios of the initial and final values of the VLD in the quantum decay $\mathcal{L}_0/\mathcal{L}_1$ and final time t_1 are given in Table I. One sees that for the largest $\mathcal{L}_0 \sim 10^6$ cm^{-2} the ratio $\mathcal{L}_0/\mathcal{L}_1$ reaches one order of magnitude. On the other hand, sometimes (e.g., set #4 with $T = 1.45$ K and smallest $\mathcal{L}_0 \simeq 6 \times 10^4$), the quantum regime of the coflow decay does not show up. The consequences of these important observations will be discussed in Sec. III.

The second step is the analysis of the later stage of the coflow turbulence decay shown by dashed-dotted lines for $T = 1.35$ and 1.45 K in Figs. 2(a) and 2(c) and fitted from time t_2 by $t^{-3/2}$ law (1b). In Table I, we present the fitting parameters b_2 and τ_2, the starting fit time t_2 together with the

ratio of the final value $\mathcal{L}_1 = \mathcal{L}(t_1)$ in the quantum fit to the initial value $\mathcal{L}_2 \equiv \mathcal{L}(t_2)$ in the classical fit.

The intermediate regime between the quantum and the classical ones [lasting from t_1 to t_2 and during which $\mathcal{L}(t)$ decays from $\mathcal{L}_1$ to $\mathcal{L}_2$] is the subject of a separate discussion in Sec. III.

Returning to the classical stage of the decay, notice that similar to the case of quantum decay, the origin time τ_2 for $\mathcal{L}_0 \sim 10^5$ is larger (closer to zero) than that for smaller $\mathcal{L}_0 \sim 10^4$, as expected from Eq. (1b). However, for larger $\mathcal{L}_0 \sim 10^6$, the time τ_2 becomes positive, which formally contradicts Eq. (1b). This can be explained assuming that there are some transient processes between quantum and classical stages of the decay that become significant for large initial values of $\mathcal{L}_0$. A possible physical reason for this will be suggested in Sec. III, after discussion of the steady-state energy spectra of quantum turbulence in the coflow.

Comparing the rates of the decay at early (quantum) and late (classical) stages in Fig. 2, one sees that classical decay is slower than the quantum one. The physical reason for that is simple: in the quantum regime the energy source in the decaying vortex tangle is relatively small with respect of its dissipation rate and may be neglected. Later, when the dissipation rate, proportional to $\mathcal{L}^2(t)$, becomes smaller, the Richardson-Kolmogorov energy cascade toward small scales, serving as an additional energy source for the vortex tangle, should be taken into account.

From the formal point of view, it looks contradictory that the $t^{-3/2}$ decay is slower than t^{-1}. This can be resolved by accounting for the interplay of the origin times in Eqs. (1). This means that $t^{-3/2}$ decay is only an intermediate regime, valid up to some large time t_3, when the increasing in time intervortex distance $\ell(t) = 1/\sqrt{\mathcal{L}(t)} \propto t^{3/4}$ becomes of the order of the largest scale Δ. We cannot observe this final stage of the decay with $\mathcal{L}(t) \sim 1$ cm^{-2}, due to a large noise level.

Nevertheless, and this is important for discussion in Sec. III, the classical $t^{-3/2}$ fit (1b) describes the observed decays during tens of seconds after t_2, when $\mathcal{L}(t)$ decreases by more than two orders of magnitude. This is seen, e.g., in Fig. 2(a) for set #3 with $T = 1.35$ K and $\mathcal{L}_0 \sim 10^6$ cm^{-2}.

2. *Counterflow and pure superflow*

Typical examples of decaying VLD in superfluid ^{4}He after switching off the counterflow are shown in Figs. 3(a) and 3(b) and after switching off pure superflow in Figs. 3(c) and 3(d). These data, obtained in 10-mm channel for $T = 1.45$ K, are very similar to the data from 7-mm channel (not discussed in this paper).

The lines are marked as for the coflow, Fig. 2, according to initial VLD: $\mathcal{L}_0 \sim 10^4$ (blue lines), $\mathcal{L}_0 \sim 10^5$ (green lines), and $\mathcal{L}_0 \sim 10^6$ (red lines). Similar to the coflow, the decay of $\mathcal{L}(t)$ may be divided into three stages: (i) The initial quantum stage that agrees with the t^{-1} fit (1a), in the time interval $0 \lesssim t \lesssim t_1$, during which $\mathcal{L}(t)$ monotonically falls from about $\mathcal{L}_0$ to $\mathcal{L}_1$. The fitting parameters b_1 and τ_1 together with the ratios $\mathcal{L}_0/\mathcal{L}_1$ and time t_1 are given in Table I. (ii) The final classical stage that agrees with the monotonic decay, described by $t^{-3/2}$ fit (1b). It starts at time $t \simeq t_2$ from the VLD $\mathcal{L}_2$ and lasts for several tens of seconds. Table I presents parameters b_2 and τ_2 together with the ratios $\mathcal{L}_1/\mathcal{L}_2$ and time t_2. (iii) The intermediate stage between the quantum and the classical one, that lasts from t_1 to t_2 and during which $\mathcal{L}(t)$ decays from $\mathcal{L}_1$ to $\mathcal{L}_2$. The most striking feature that qualitatively differs this stage in counterflow and pure superflow from that in coflow is the nonmonotonic character of the decay, clearly seen in Fig. 3, especially for large $\mathcal{L}_0$.

Comparing Fig. 2 for coflow with Fig. 3 for counterflow and pure superflow, one sees that there are no qualitative differences between all these flows at the initial quantum and final classical stages of the monotonic decay of VLD. The same conclusion follows from Table I, which demonstrates only a small quantitative difference between these flows at these stages, perhaps with some scattered values of displayed parameters for all flows.

As we discussed above, the counterflow and pure superflow qualitatively differ from the coflow only at the intermediate stage, demonstrating nonmonotonic decay. As we explain below, this difference is a consequence of a very different character of the steady-state energy spectra (energy distribution between scales) in the counterflow and pure superflow with nonzero values of the counterflow velocity $U_{ns} \neq 0$ from the stationary spectrum in the coflow, for which $U_{ns} = 0$. The energy spectra of quantum ^{4}He turbulence for all three types of flows, discussed in our paper, are the subject of Sec. II C.

C. On energy spectra of superfluid turbulence

1. *Coflow*

In coflow turbulence, the mean velocity profiles of the normal and superfluid velocity $\boldsymbol{U}_n(y)$ and $\boldsymbol{U}_s(y)$ practically coincide almost everywhere in the channel, perhaps except for narrow regions near the walls, because the pressure drop is the same for both fluid components. The relatively large mutual friction tries to lock the mean normal and superfluid velocities and only kinematic viscosities, important in the near-wall region (viscous and buffer layers) are different: $\nu_n \neq \nu_s = 0$. Thus, the energy spectra of the normal and superfluid components $\mathcal{E}_n$ and $\mathcal{E}_s$ practically coincide in the entire energy containing and inertial intervals of scales. Ignoring unessential for present discussion intermittency effects, we can use classical K41 energy spectra for both ^{4}He components [27], shown in the left part in Fig. 4(a):

$$\mathcal{E}_n = \mathcal{E}_s \simeq C_{K41}\varepsilon^{2/3}k^{-5/3} \,. \tag{3}$$

Here, $\varepsilon_n = \varepsilon_s \equiv \varepsilon$ are the corresponding energy fluxes over inertial interval of scales and $C_{K41} \simeq 1.4$ is the Kolmogorov constant.

Using K41 energy spectrum (3), we can estimate the classically generated VLD $\mathcal{L}_*$ originated from its large-k part. This part turns out to be significantly smaller than the experimentally observed steady-state VLD $\mathcal{L}_0$. To explain why $\mathcal{L}_* \ll \mathcal{L}_0$, one should find some additional mechanism of vortex generation aside from the classical flow instabilities in the channel flow. Such a mechanism may be provided by the difference between the normal and the superfluid velocities. The normal and superfluid energy spectra deviate from each other in the crossover region $k\ell \sim 1$ [28,29]. The velocity coupling is also violated in the narrow region near the channel walls and near the surface of the grid at the channel

entrance, where normal and superfluid components satisfy different boundary conditions. In these areas, the velocities of components differ and excite a random vortex tangle leading to a peak in the energy spectrum near the crossover scale.

Therefore, the resulting turbulent energy spectrum $\mathcal{E}(k)$ may include, in addition to the classical K41 region Eq. (3) (spanning scales from the integral length scale Δ down to the intervortex distance ℓ), also a quantum contribution $\mathcal{E}_s^Q(k)$, which has a form of a peak at scales close ℓ, corresponding to the random tangle of quantized vortex lines. This peak has large-k asymptote $\propto 1/k$ originating from the velocity field near the quantized vortex lines. In the region of $k < \pi/\ell$, the quantum peak is adjoined by the classical region with the thermodynamic equilibrium spectrum $\propto k^2$, describing equipartition of energy between degrees of freedom [30] [see Fig. 4(a)].

2. *Counterflow and pure superflow*

Notice that in the steady-state regimes of the counterflow and pure superflow, the energy spectrum of the superfluid component has a qualitatively different form from that in the coflow, as sketched in Fig. 4(b). The physical reason for that is the decoupling of the normal and superfluid turbulent velocity fluctuations, caused by the nonzero value of the counterflow velocity $\boldsymbol{U}_{ns}$ in the counterflow and superflow, while in the coflow $\boldsymbol{U}_{ns} = 0$ [31].

In the analytical theory of counterflowing turbulence presented in Sec. IV, we show that on a qualitative level the resulting energy spectra are similar to those in ^{3}He-B turbulence with the normal fluid component at rest studied in Refs. [32,33]. We use these spectra as a basis for our numerical analysis. The analytical form of the energy spectra found by L'vov, Nazarenko, and Volovik (LNV) [32] in current notations reads as

$$\mathcal{E}(k) = \mathcal{E}_0 \left(\frac{k_0}{k}\right)^3 \left[\left(1 - \frac{\Omega}{\Omega_{cr}}\right)\left(\frac{k}{k_0}\right)^{2/3} + \frac{\Omega}{\Omega_{cr}}\right]^2, \quad (4a)$$

$$\Omega_{cr} = \frac{5}{4}\sqrt{k_0^3\,\mathcal{E}_0}\,, \quad \Omega = \alpha(T)\kappa\mathcal{L}\,. \quad (4b)$$

Here, Ω is the mutual friction frequencies for the superfluid and $\alpha(T)$ is the dimensionless mutual friction parameter, tabulated in Ref. [26].

At $\Omega = \Omega_{cr}$ spectrum (4a) becomes the scale-invariant "critical" spectrum

$$\mathcal{E}_{cr}(k) = \mathcal{E}_0 \left(\frac{k_0}{k}\right)^3, \quad \text{LNV critical.} \quad (5)$$

For $\Omega < \Omega_{cr}$, solution (4a) can be considered as "subcritical" and written as follows:

$$\mathcal{E}_{sb}(k) = \mathcal{E}_0 \frac{k_0^3}{k^{5/3}}\left[\frac{1}{k^{2/3}} + \frac{1}{k_{cr}^{2/3}}\right]^2, \quad \text{LNV subcritical,}$$

$$k_{cr} = k_0 \left(\frac{\Omega}{\Omega_{cr} - \Omega}\right)^{3/2}. \quad (6)$$

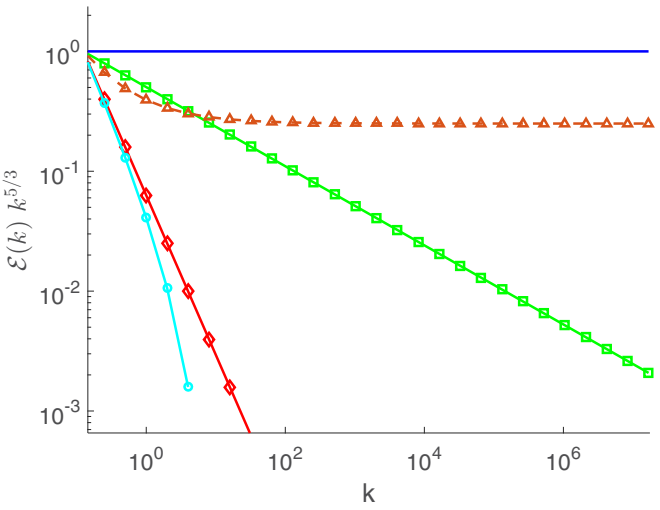

FIG. 5. Five variants of the stationary energy spectra, compensated by $k^{5/3}$, $k^{5/3}E_s(k)$, serving as the initial conditions for the Sabra decay [Eq. (A2)]: (a) K41 energy $E_{0,a} \propto k^{-5/3}$ [Eq. (3)] (solid blue line); (b) experimental counterflow spectrum $E_{0,b}(k) \propto k^{-2}$, reported in [39] (green line with squares); (c) critical LNV spectrum [Eq. (5)] $E_{0,d}(k) \propto k^{-3}$ (red line with diamonds); (d) supercritical LNV spectrum $E_{0,d}(k) = 0$ for $k > k_*$ [Eq. (7)] (light blue line with circles); (e) subcritical LNV spectrum [Eq. (6)] (brown line with triangles).

In the case $\Omega > \Omega_{cr}$, Eq. (4a) can be considered as "supercritical" spectrum

$$\mathcal{E}_{sp}(k) = \mathcal{E}_0 \frac{k_0^3}{k^{5/3}}\left[\frac{1}{k^{2/3}} - \frac{1}{k_*^{2/3}}\right]^2, \quad \text{LNV supercritical,}$$

$$k_* = k_0 \left(\frac{\Omega}{\Omega - \Omega_{cr}}\right)^{3/2}. \quad (7)$$

Examples of the three versions of the LNV spectra are plotted in Fig. 5. Aside from this classical part, the spectrum includes a quantum peak, shown in Fig. 4(b), that is presumably more pronounced than the peak in the coflow, shown in Fig. 4(a). These peaks have similar structure: large-k asymptotics $\propto 1/k$ and small-k asymptotics $\propto k^2$.

III. BASIC AND IMPROVED MODELS OF DECAYING QUANTUM TURBULENCE

In this section, we first propose and solve a basic model of the VLD evolution $\mathcal{L}(t)$ in decaying quantum turbulence. The model can then be further developed to clarify the experimental facts in more detail.

A. Basic model of decaying coflow turbulence

Assume that the time derivative of $\mathcal{L}(t)$ consists of a simple sum of the quantum decay term $-\eta_{qn}$ and the classical source term η_{cl}, neglecting possible processes of their interaction:

$$\frac{d\mathcal{L}(t)}{dt} = -\eta^Q + \eta^{cl}\,. \quad (8)$$

The quantum tangle decay (without counterflow velocity) is usually discussed in the framework of the Vinen equation

[14,20] with the (quantum) decay term $\eta^{\rm Q} = \chi_2 \kappa \mathcal{L}^2/(2\pi)$. Estimating the phenomenological coefficient χ_2 in the local induction approximation [34,35], we rewrite $\eta^{\rm Q}$ in terms of the dimensionless mutual friction parameter α and, the vortex line curvature $\widetilde{S}$, normalized by the intervortex distance ℓ, $c_2 \sim 1$:

$$\eta^{\rm Q} \simeq \alpha\, \kappa\, c_2^2 \Lambda \mathcal{L}^2/(4\pi), \quad c_2 \equiv \widetilde{S}\ell, \quad \Lambda = \ln(\ell/a_0). \tag{9a}$$

Since for our conditions the parameter $\Lambda/(4\pi) \simeq 1$ varies from 0.9 to 1.1 and $c_2 \simeq 1$ depends weakly on temperature [36], we can simplify this relation by introducing a dimensionless fitting parameter d_1, and write

$$\eta^{\rm Q} = \alpha\, \kappa \mathcal{L}^2/d_1. \tag{9b}$$

With this $\eta^{\rm Q}$ and without classical source term $\eta^{\rm cl}$, Eq. (8) has well-known t^{-1} solution (1a) with

$$b_1 = d_1/(\alpha\ \kappa \mathcal{L}_0 \tau_1). \tag{10}$$

The positive contribution $\eta^{\rm cl}$ in the right-hand side of Eq. (8) originates from the direct energy flux ε from the classical energy containing scale $k\Delta \sim 1$, to the quantum energy peak $\mathcal{E}^{\rm Q}(k)$, located at $k\ell \sim 1$ (see Fig. 4). To estimate $\eta^{\rm cl}$, recall that $\mathcal{E}^{\rm Q} \sim \kappa^2 \mathcal{L}$ (see also Ref. [37]). Therefore, the flux of VLD from the classical scales to the quantum energy peak may be estimated as

$$\eta^{\rm cl} \simeq \varepsilon/\kappa^2. \tag{11}$$

Integrating Eq. (3) for the energy spectra, we find the total classical kinetic energy

$$\mathcal{E}^{\rm cl} = \int \mathcal{E}^{\rm cl}(k)\, dk \simeq C_{\rm K41} \varepsilon^{2/3} \int_{\pi/\Delta}^{\pi/\ell} k^{-5/3} dk$$
$$= \frac{3\, C_{\rm K41} \varepsilon^{2/3}}{2\pi^{2/3}} [\Delta^{2/3} - \ell^{2/3}] \simeq \left(\frac{\varepsilon\, d_2 \Delta}{2}\right)^{2/3}. \tag{12}$$

Here, we roughly estimated lower and upper limits of the inertial interval as π/Δ and π/ℓ. Taking into account that at our experimental conditions Δ significantly exceeds ℓ, we neglected ℓ with respect to Δ. Finally, we replaced in Eq. (12) all numerical factors by a new fitting dimensionless constant $d_2 \simeq 1$. As a result,

$$\varepsilon \simeq 2\, (\mathcal{E}^{\rm cl})^{3/2}/(d_2 \Delta). \tag{13}$$

Now, we can write the classical energy balance equation

$$\frac{d\mathcal{E}^{\rm cl}}{dt} = -\varepsilon = -2\frac{(\mathcal{E}^{\rm cl})^{3/2}}{d_2 \Delta}, \tag{14}$$

with the solution

$$\mathcal{E}^{\rm cl}(t) = \left(\frac{d_2 \Delta}{t - \tau_2}\right)^2, \quad \tau_2 = \frac{d_2 \Delta}{\sqrt{\mathcal{E}_0^{\rm cl}}}, \tag{15}$$

where $\mathcal{E}_0^{\rm cl}$ is the initial energy at $t = 0$. Together with Eqs. (13) and (11), this finally gives

$$\eta^{\rm cl}(t) = \frac{\varepsilon^{\rm cl}(t)}{\kappa^2} = \frac{2(d_2\Delta)^2}{(t - \tau_2)^3}. \tag{16}$$

Collecting Eqs. (8), (9b), (15), and (16), we finally suggest a simple model of the VLD decay in the form

$$\frac{d\mathcal{L}}{dt} = \frac{2\,(d_2\Delta)^2}{\kappa^2 (t - \tau_2)^3} - \frac{\alpha\, \kappa}{d_1} \mathcal{L}^2. \tag{17}$$

Here, d_1 and d_2 are dimensionless phenomenological parameters. Note that τ_2 is of the order of turnover time $\tau_\Delta \simeq \Delta/\sqrt{\mathcal{E}_0^{\rm cl}}$ of the largest (energy-containing) eddies in the flow.

When the classical energy $\mathcal{E}_0^{\rm cl}$ is small, the virtual origin time τ_2, according to Eq. (15), is large and the first term in the right-hand side of Eq. (17) may be neglected. In this case, Eq. (17) may be easily solved, giving t^{-1} decay $\mathcal{L}^{\rm Q}$ [Eq. (1a)]. Assume now that for large times the time derivative $d\mathcal{L}/dt$ in Eq. (17) may be neglected. Then, Eq. (17) reproduces $t^{-3/2}$ decay $\mathcal{L}^{\rm cl}$ [Eq. (1b)] with

$$d_2 = b_2 \frac{(\kappa\, \tau_2)^{3/2}}{\Delta} \mathcal{L}_0 \sqrt{\frac{\alpha}{2 d_1}} \tag{18a}$$

or by using d_1 from Eq. (10):

$$d_2 = b_2 \frac{\kappa\, \tau_2^{3/2}}{\Delta} \sqrt{\frac{\mathcal{L}_0}{2 b_1 \tau_1}}. \tag{18b}$$

Neglecting for simplicity the time dependence of the first term in the right-hand side of Eq. (17), one can solve it exactly with the result

$$\mathcal{L}(t) = \mathcal{L}^{\rm cl}(t) \coth\left[\frac{\mathcal{L}^{\rm cl}(t)}{\mathcal{L}^{\rm Q}(t)}\right]. \tag{19}$$

Remind that $\lim_{x\to 0} \coth[x] \to 1/x$, $\lim_{x\to\infty} \coth[x] \to 1$. Therefore, when $\mathcal{L}^{\rm Q} \gg \mathcal{L}^{\rm cl}$, $\mathcal{L}(t) \to \mathcal{L}^{\rm Q}$. Otherwise, in the limit $\mathcal{L}^{\rm Q} \ll \mathcal{L}^{\rm cl}$, $\mathcal{L}(t) \to \mathcal{L}^{\rm cl}$. For $\mathcal{L}^{\rm Q} \sim \mathcal{L}^{\rm cl}$, the function $\mathcal{L}(t)$ describes a smooth transition between $\mathcal{L}^{\rm Q}$ and $\mathcal{L}^{\rm cl}$, being always larger than both $\mathcal{L}^{\rm Q}$ and $\mathcal{L}^{\rm cl}$. In this way, the approximate solution (19) for $\mathcal{L}(t)$ interpolates the solution of the model (17) between the small- and large-time asymptotes.

Even better interpolation between exact asymptotes $\mathcal{L}^{\rm Q}$ and $\mathcal{L}^{\rm cl}$ gives the following modification of Eq. (19):

$$\bar{\mathcal{L}}(t) = \mathcal{L}^{\rm cl}(t) \coth\left[\frac{\mathcal{L}^{\rm cl}(0)}{\mathcal{L}^{\rm Q}}\right]. \tag{20}$$

Having in mind the approximate character of the evolution model (17), we consider Eq. (20) for $\bar{\mathcal{L}}(t)$ as an analytical form of the VLD time dependence $\mathcal{L}(t)$, practically equivalent to the suggested basic model of decaying superfluid turbulence.

B. Analysis of the decay fitting parameters

The $\mathcal{L}_0$ dependencies of the fitting parameters τ_1 and τ_2, b_1 and b_2, d_1 and d_2 for three different types of the flow are given in Table I. For clarity, we additionally display these dependencies in Fig. 6.

1. Quantum and classical origin times τ_1 and τ_2

The dependence of the quantum origin times τ_1 on the initial VLD $\mathcal{L}_0$ for coflow, counterflow, and pure superflow is shown in Fig. 6(a). As expected from Eqs. (1a) and (10), the values of τ_1 for coflow are negative and monotonically increase with $\mathcal{L}_0$. There, values of τ_1 for coflow are clearly different

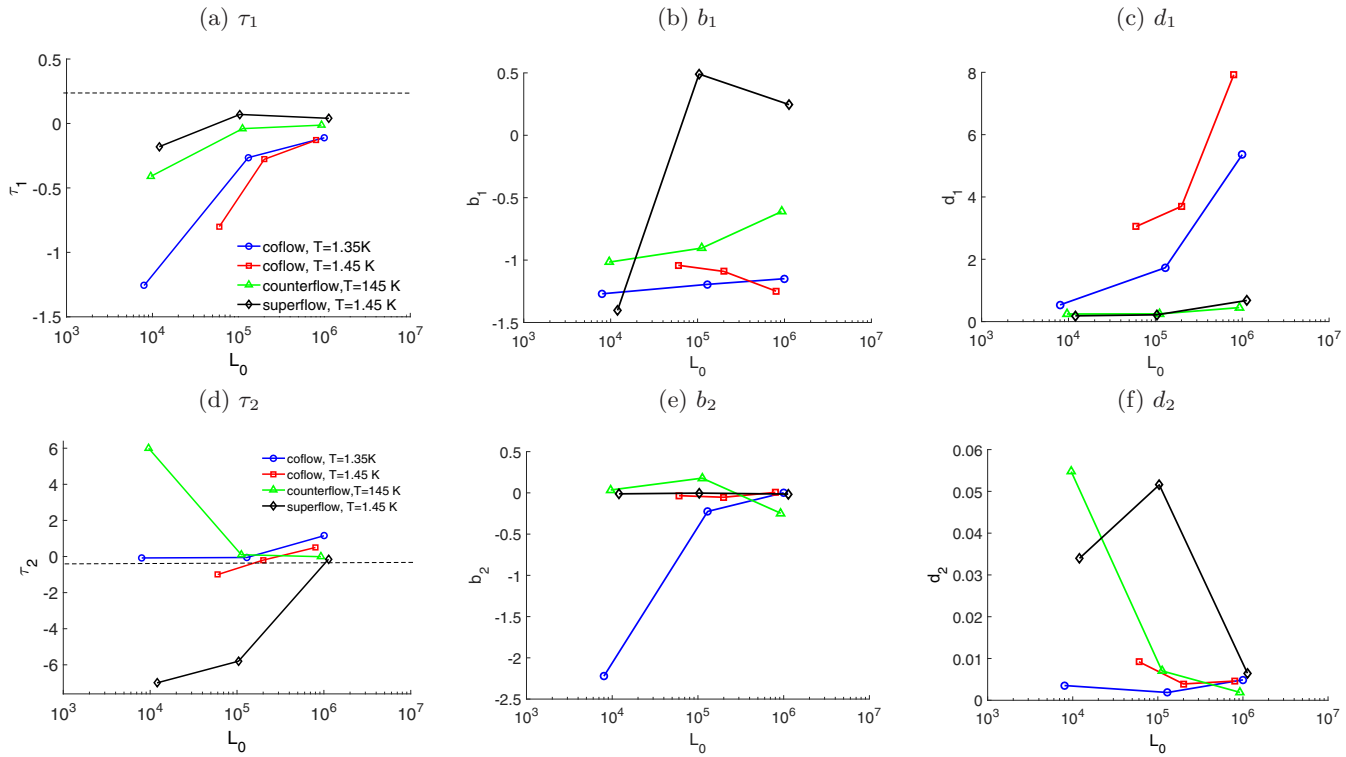

FIG. 6. Virtual origin times τ_1 and τ_2 for the quantum (1a) (a) and classical (1b) decay (d) vs initial VLD $\mathcal{L}_0$ in initial coflow, counterflow, and pure superflow. Panels (b) and (e) display $\mathcal{L}_0$ dependence of the b_1 and b_2 fit parameters. Panels (c) and (f) display $\mathcal{L}_0$ dependence of the d_1 and d_2 fit parameters. The numerical values of all these parameters are given in Table I.

from those in the counterflow and pure superflow, especially for smaller $\mathcal{L}_0$. This is related to the fact that in the coflow, the classical energy flux towards the quantum vortex tangle is present from the very beginning of the decay (at $t = 0$), while in the counterflow and pure superflow it appears only after some delay, required for developing the Kolmogorov cascade from the initial spectrum sketched in Fig. 4(b).

As expected, the classical origin time τ_2 tends to decrease for larger $\mathcal{L}_0$, as depicted in Fig. 6(d). The most striking fact, seen in Fig. 6(d), is that τ_2 can be positive. This definitely contradicts the basic model of $\mathcal{L}(t)$ decay, formulated in Sec. III A. Nonmonotonic evolution of $\mathcal{L}(t)$, clearly seen in Fig. 3, also calls for improvements of the basic model of $\mathcal{L}(t)$ decay, in order to account for the time delay of the energy flux into the quantum vortex tangle. This is done in Sec. III D, prefaced by Sec. III C, devoted to the study of the energy-flux delay in the decaying turbulence in counterflow and pure superflow, caused by the later development of the Richardson-Kolmogorov cascade from the localized energy spectra.

2. *Quantum and classical parameters b_1, d_1 and b_2, d_2*

The $\mathcal{L}_0$ dependencies of the fit parameters b_1, d_1 and b_2, d_2 are shown in Figs. 6(b), 6(c), 6(e) and 6(f). Quantum parameters $b_1, d_1 \sim O(1)$; their deviation from unity reflects the nonuniversal character of the transient regime after switching off the flow: the mean velocity has to relax to zero, anisotropic statistics of the vortex tangle, affected by the mean flow, has to become isotropic, etc. We will not discuss these complicated issues in this paper, as they do not seem to contribute to better understanding of the basic physical picture of decaying quantum turbulence in three types of the flow.

The same can be said about the scatter of values of the classical fitting parameters b_2, d_2 for different types of the flow. Notice only that their values, being much smaller than unity, become even smaller for larger $\mathcal{L}_0$. The same tendency is demonstrated by the ratio $\mathcal{L}_2$ (from which the classical decay begins) to the initial value of VLD $\mathcal{L}_0$. This may be easily interpreted in the following way: the random vortex tangle decays according to the quantum t^{-1} law as long as the energy influx from the classical part of superfluid turbulence may be neglected. This holds as long as the tail of classical energy spectrum $\mathcal{E}_s^{K41}(\pi/\ell)$ is smaller than the quantum energy spectrum $\mathcal{E}_s^{Q}(\pi/\ell)$ at this scale. Therefore, the ratio $\mathcal{E}_s^{Q}(\pi/\ell)/\mathcal{E}_s^{K41}(\pi/\ell)$ may be roughly estimated as $1/b_2 \gg 1$ or as a value between the ratios $\mathcal{L}_0/\mathcal{L}_1$ and $\mathcal{L}_0/\mathcal{L}_2$ (remind that $\mathcal{L}_1$ is the VLD at which the quantum decay terminates). As shown in Table I, both ratios are much larger than unity and both tend to increase for larger $\mathcal{L}_0$.

Based on this analysis, we conclude that the quantum peak of energy at the intervortex scale ℓ, as a rule, dominates over the tail of classical energy spectrum at this scale, as depicted in Fig. 4. Notice that, generally speaking, this qualitative conclusion may be guessed just from the observation of the decay laws, shown in Fig. 2. What is added by our analysis is a semiquantitative estimate of the ratio $\mathcal{E}_s^{Q}(\pi/\ell)/\mathcal{E}_s^{K41}(\pi/\ell)$.

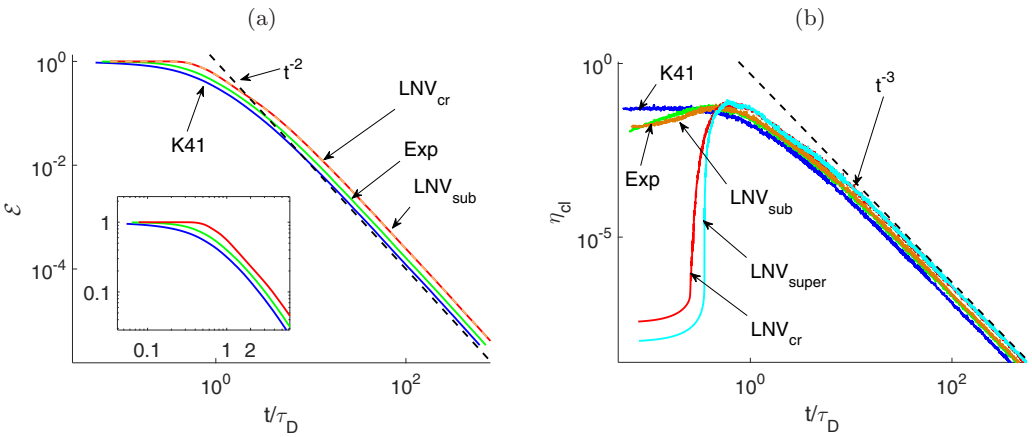

FIG. 7. (a) Time dependence of the total energy $\mathcal{E}(t)$ in decaying superfluid turbulence from different initial conditions, shown in Fig. 5. The inset shows the short-time evolution of the total energy $\mathcal{E}(t)$. (b) Time dependence of the rate of energy dissipation $\varepsilon(t)/\kappa^2$ that plays role of the VLD flux $\eta^{\rm cl}(t)$ in the model (8). The lines are colored as in Fig. 5 without markers. In (a), the lines for critical and subcritical LNV spectra coincide. The lines for experimental and supercritical LNV spectra almost coincide.

C. Energy-flux delay in the decaying counterflow turbulence

It is commonly accepted that the Richardson-Kolmogorov cascade develops from any localized in the k-space initial state over finite time, of the order of a few turnover times of the energy-containing eddies. Nevertheless, the details of the transient regime and how they depend on the initial state are poorly understood. In order to clarify the law of delay in "switching on" the energy flux $\varepsilon_{\rm cl}(t)$ [Eq. (16)] that contributes to the right-hand side of the basic model (17), we adopt in our paper so-called Sabra-shell model of turbulence, successfully utilized in studies of quantum turbulence, e.g., in Refs. [29,33,38].

The required version of the Sabra model and the numerical procedure are described in Appendix A. Here, we present only results of the time evolution of the energy spectrum $E_{\rm s}(k_m,t) = \langle|u_m|^2\rangle/k_m$ in the decaying quantum turbulence from five types of the initial conditions $E_{\rm s}(k,0) \equiv E_0(k)$, shown in Fig. 5:

ICa: K41 energy spectrum [Eq. (3)] $E_{0,a}(k) \propto k^{-5/3}$;

ICb: experimental counterflow spectrum $E_{0,b}(k) \propto k^{-2}$, reported in Ref. [39];

ICc: critical LNV spectrum [32] $E_{0,c}(k) \propto k^{-3}$ [Eq. (5)];

ICd: supercritical LNV spectrum [Eq. (7)] $E_{0,d}(k) = 0$ for $k > k_*$;

ICe: subcritical LNV spectrum [Eq. (6)] $E_{0,e}(k)$.

The time dependence of the total energy for five types of the initial conditions (a)–(e) are shown in Fig. 7(a). As expected, in all cases the large-time asymptotics $E(t) \propto t^{-2}$ agrees with Eq. (15) (see black dashed line). What is important for current discussion is the small-time behavior for t below few τ_Δ, shown in the inset of Fig. 7(a). Clearly, for critical and supercritical initial conditions ICc and ICd, the energy $\mathcal{E}(t)$ (shown by coinciding solid red and dashed light blue lines) does not decay up to $t \approx \tau_\Delta$. This is the time required for development of the Richardson-Kolmogorov cascade, transferring energy into the dissipative range of scales (large k).

On the contrary, for the K41 initial condition, ICa, the energy decays from the very beginning [see blue solid line in the inset of Fig. 7(a)]. This behavior is also expected. For two intermediate initial conditions, ICb and ICe, the initial energy is also localized in the region of small k, but not so strongly, as in ICc and ICd cases. Accordingly, the time dependence of $E(t)$ for ICb and ICe cases, shown by green and orange lines, demonstrates intermediate behavior.

All these features are clearly seen in Fig. 7(b), showing the time dependence of the rate of energy dissipation $\varepsilon(t)$. In our simulation we used a very small value of the kinematic viscosity, therefore, $\varepsilon(t)$ is actually a measure of the energy flux via crossover wave number $\sim 1/\ell$ that serves as the energy flux from classical to quantum scale range. Thus, according to Eq. (11), we can say that the time dependence $\varepsilon(t)$ actually gives the time dependence of the important ingredient of the model (8), the classical energy source $\eta^{\rm cl}(t) \simeq \varepsilon(t)/\kappa^2$.

All plots of $\eta^{\rm cl}(t)$ in Fig. 7(b) have t^{-3} asymptote for large t, in agreement with Eq. (16). Moreover, for the K41 initial conditions ICa expected in coflow decay, and shown by the blue line, Eq. (16) provides reasonable fit of $\eta^{\rm cl}(t)$ for all times, as shown by the solid black line in Fig. 7. Thus, our numerical simulations support the basic model (17) of the decay in coflow (see Sec. III A).

The situation is completely different for other initial conditions, expected for the counterflow and pure superflow cases. There is the most striking difference for the well-localized, critical, and supercritical ICc and ICd, shown in Fig. 7 by (practically coinciding) red and light blue lines. One sees that for small time $\eta^{\rm cl}(t) \approx 0$, then it is sharply switching on and after few turnover times τ_Δ reaches the "basic" behavior (16). This can be accounted for by "improving" the basic model, introducing into Eq. (16) for the classical source term the time delay function $F_{\rm del}(t)$:

$$\eta^{\rm cl} = \frac{2(d_2\,\Delta)^2}{(t+\tau_{\rm del}-\tau_2)^3} \Rightarrow F_{\rm del}(t)\,\frac{2(d_2\,\Delta)^2}{(t-\tau_2)^3}. \tag{21a}$$

It is convenient to choose $F_{\rm del}(t)$ as a square of new function $f_n(t)$ that has a simple form

$$F_{\rm del}(t) = f_n^2(t), \quad f_n(t) = \frac{t^n}{t^n+\tau_{\rm del}^n}. \tag{21b}$$

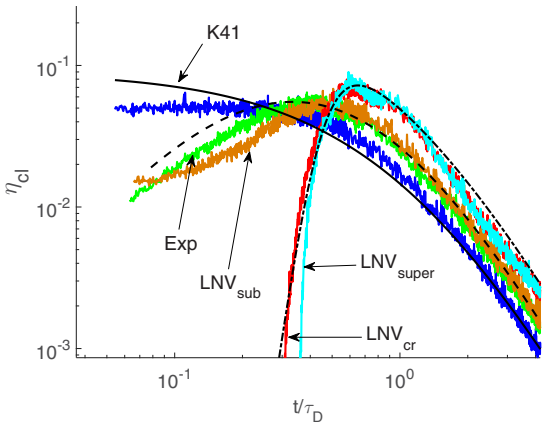

FIG. 8. The details of the short-time dependence of the rate of energy dissipation $\varepsilon(t)/\kappa^2$, shown in Fig. 7(b). Black solid line: the basic model dependence (16) for $\eta^{cl}(t)$ fits K41 initial conditions ICa. Black dashed line shows improved model dependence (21) with $n = 2$; it approximates numerically found $\eta^{cl}(t)$ for weakly localized initial conditions ICb and ICe. Black dotted-dashed line, given by (21) with $n = 6$, fits $\eta^{cl}(t)$ computed with strongly localized initial conditions ICc and ICd.

As required, $f_n(t) \to 1$ for $t \to \infty$. Generally speaking, $f(0) = 0$ only for the supercritical case ICd. For all other cases (except for the K41 spectrum, which we are not discussing here) $f(0) \neq 0$, although small. This difference is not important for us and for simplicity we adopted in Eq. (21b) a simple assumption that $f_n(0) = 0$. The delay time τ_{del} in Eq. (21b) is expected to be about the largest eddies turnover time τ_Δ. Indeed, as seen in Fig. 8, $\tau_{del} \simeq 0.4\tau_\Delta$.

Notice that the parameter n in Eq. (21b), responsible for the sharpness of the delay function, is different for different initial conditions. Figure 8 demonstrates that for the weakly localized initial conditions ICb and ICe, a reasonable approximation to the numerical observation can be reached with $n = 1$, while for strongly localized initial conditions a good fit corresponds to $n = 6$.

D. Improved model of VLD decay vs experiment

1. Improving the basic model by the energy-flux delay

In the previous Sec. III C we improved the classical source term accounting for the time delay by the delay function $F_{del}(t)$. Substituting the new form (21) of η^{cl} in the basic model (17), we formulate the "improved decay model" of quantum turbulence:

$$\frac{d\mathcal{L}}{dt} = \frac{2\,(d_2\Delta)^2 F_{del}(t)}{\kappa^2(t + \tau_{del} - \tau_2)^3} - \frac{\alpha\,\kappa}{d_1}\mathcal{L}^2. \tag{22}$$

For $\tau_{del} = 0$ the improved model (22) coincides with the basic model (17). For $t < \tau_{del}$, the delay function (21b) $F_{del}(t) < 1$ and the energy-flux term in Eq. (22), that is proportional to $F(t)$, is suppressed. For $t \sim \tau_{del}$, this term is gradually switching on and, finally, for $t \gg \tau_{del}$ the improved and basic models (22) and (17) again coincide.

By analogy with Eq. (20), we can formulate the analytical form of the improved decay model:

$$\tilde{\mathcal{L}}(t) = f_{del}(t)\mathcal{L}^{cl}(t + \tau_{del}) \coth\left[\frac{f_{del}(t)\mathcal{L}^{cl}(0)}{\mathcal{L}^{Q}}\right]. \tag{23}$$

Now we are fully armed to compare in the two following sections the suggested analytical models (20) and (23) with experimental observations.

2. Basic decay model vs coflow experiment

We begin here with the more simple coflow case, choosing for comparison the less noisy set #3, demonstrating (red line) in Fig. 2(a) the decay of almost four decades over 50 s. This line is reproduced (in red) in Fig. 9(a) together with the plot of analytical $\bar{\mathcal{L}}(t)$ (shown by the blue dotted line), predicted by the basic model. This line is barely seen because it practically coincides with the red experimental line within the linewidth, broadened after 25 s by noise. Some discrepancy between the experiment and the model prediction is better seen on the closeup Fig. 9(b) showing the first 5 s of the decay.

Notice that the basic model is very simple: it completely ignores any interaction between the quantum peak and the classical large-scale turbulence. In formulating the model we also ignored the energy stored in the equilibrium part of the

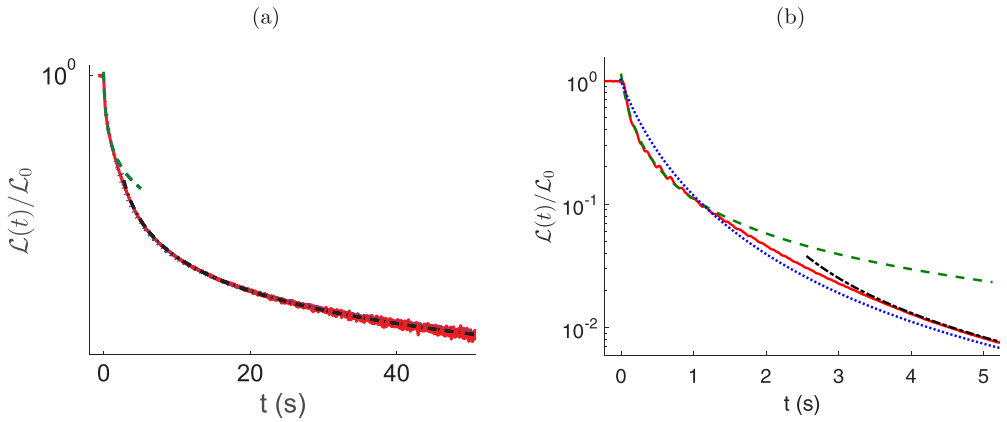

FIG. 9. Comparison of the experimental observation of coflow decay with the basic model predictions. Red solid lines, reproduced from red lines in Figs. 2(a) and 2(b), show the coflow data for set #3 ($T = 1.35$ K, $\mathcal{L}_0 \approx 10^6$ cm^{-2}). Blue dotted lines show basic model prediction $\bar{\mathcal{L}}(t)$ [Eq. (20)] with $\tau_1 = 0.5$ s, $\tau_2 = 1$ s, and $b_2 = 0.075$.

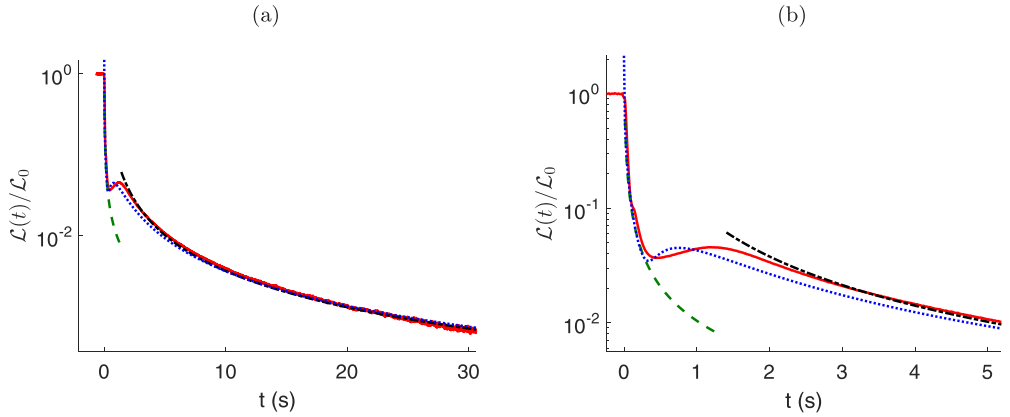

FIG. 10. Comparison of the experimental observation for the superflow with the improved model predictions. Red solid lines, reproduced from red lines in Figs. 3(c) and 3(d) for superflow #12 ($T = 1.45$ K, $\mathcal{L}_0 \approx 10^6$ cm^{-2}). Blue dotted lines show improved model prediction $\tilde{\mathcal{L}}(t)$ [Eq. (23)] with $n = 2$, $\tau_1 = 0.015$ s , $\tau_2 = 0.1$ s, $\tau_{\rm dec} = 0.6$ s, and $b_2 = 0.22$.

classical energy $\mathcal{E}_{\rm s}^{\rm TD}$. Last but not least, the model does not account for the spatial inhomogeneity of the turbulent channel flow, in which turbulent kinetic energy significantly depends on the distance to the walls. Bearing all these in mind, we consider the agreement between the experiment and the model quite satisfactory.

3. *Improved decay model vs counterflow experiment*

Our next step is a discussion of the decay in the counterflow and pure superflow cases. For our rather simplified manner of modeling, there is no physical difference between the counterflow and pure superflow decaying turbulence. Therefore, from the data presented in Fig. 3, we chose the set #12 (superflow at $T = 1.45$ K, $\mathcal{L}_0 \simeq 10^6$ cm^{-2}) shown in Figs. 3(c) and 3(d) by red lines. In this case, the noise is relatively low and the bump on the $\mathcal{L}(t)$ dependence is clearly pronounced. Red lines in Figs. 10(a) and 10(b) reproduce the experimental results shown in Figs. 3(c) and 3(d) in red. Blue dotted lines result from the analytical form $\tilde{\mathcal{L}}(t)$ of the improved model of decay, given by Eq. (23) with $n = 2$, $\tau_1 = 0.015$ s, $\tau_2 = 0.1$ s, $b_2 = 0.22$.

Semiquantitative agreement between experimental observation and the improved decay model allows us to conclude that this model reflects the basic physical mechanisms responsible for the time dependence of the VLD. In particular, it accounts for the time delay in the delivery of the energy flux from classical to quantum parts of superfluid turbulence.

IV. TOWARDS THEORY OF QUANTUM TURBULENCE WITH COUNTERFLOW

In mechanically driven quantum turbulence, the mean velocities of the normal and superfluid components are known to coincide: $\boldsymbol{U}_{\rm n} = \boldsymbol{U}_{\rm s}$. Numerous laboratory, numerical and analytical studies showed that under these conditions the mutual friction between the normal and superfluid velocity components couple also their fluctuations: $\boldsymbol{u}_{\rm n}(\boldsymbol{r},t) \approx \boldsymbol{u}_{\rm s}(\boldsymbol{r},t)$ almost at all scales. This is not the case in thermally driven quantum turbulence, where the counterflow velocity $\boldsymbol{U}_{\rm ns} \neq 0$ partially decouples the normal and superfluid velocity fluctuations and enhances the turbulent energy dissipation due to the mutual friction. In this section, we suggest a simple analytical model of the resulting energy balance in counterflow turbulence that predicts dramatic suppression of the energy spectrum at intermediate and small scales.

A. Differential model for the energy spectra

The evolution equations for one-dimensional (1D) energy spectra $\mathcal{E}_{\rm s}(k,t)$ and $\mathcal{E}_{\rm n}(k,t)$, defined by Eqs. (B5), were derived in Ref. [31]:

$$\frac{\partial \mathcal{E}_{\rm s}(k,t)}{2\,\partial t} + \mathcal{NL}_{\rm s} = \Omega[\mathcal{E}_{\rm ns}(k,t) - \mathcal{E}_{\rm s}(k,t)], \tag{24a}$$

$$\frac{\partial \mathcal{E}_{\rm n}(k,t)}{2\,\partial t} + \mathcal{NL}_{\rm n} = \Omega_{\rm n}[\mathcal{E}_{\rm ns}(k,t) - \mathcal{E}_{\rm n}(k,t)]. \tag{24b}$$

Nonlinear terms $\mathcal{NL}_{\rm s,n}$ conserve kinetic energy and therefore may be presented in the divergent form

$$\mathcal{NL}_{\rm s} = \frac{d\varepsilon_{\rm s}}{dk}, \quad \mathcal{NL}_{\rm s} = \frac{d\varepsilon_{\rm s}}{dk}. \tag{25a}$$

In these expressions, $\varepsilon_{\rm s}(k)$ and $\varepsilon_{\rm n}(k)$ are the energy fluxes over scales in corresponding subsystems that can be expressed in the terms of the third-order correlation function of $\boldsymbol{u}_{\rm s}(k)$ exactly as in classical turbulence. In order to proceed further, one can borrow a closure procedure from classical turbulence that expresses $\varepsilon_{\rm s}(k)$ in terms of the energy spectrum $\mathcal{E}_{\rm s}(k)$. Even though this step is widely used, it is worth remembering that it is uncontrolled. The simplest algebraic closure relation suggested by Kovasznay [40],

$$\varepsilon_{\rm s}(k) \simeq \tfrac{5}{8} k^{5/2} \mathcal{E}_{\rm s}^{3/2}(k), \tag{25b}$$

just follows from the K41 dimensional reasoning

$$\mathcal{E}_{\rm s}(\varepsilon|k) = C_{\rm K} \varepsilon^{2/3} k^{-5/3}, \quad C_{\rm K} = (8/3)^{2/3} \approx 1.4. \tag{25c}$$

Equations (24) involve the cross correlation $\mathcal{E}_{\rm ns}(k)$, defined by Eqs. (B5). The analytical theory of the coupling-decoupling processes [31], using Langevin inspired approach to model the nonlinear term, results in the analytical expression for $\mathcal{E}_{\rm ns}(k)$ in terms of $\mathcal{E}_{\rm s}(k)$ and $\mathcal{E}_{\rm n}(k)$. Using Eqs. (13) and (16) from Ref. [31], the result in our experiments range of parameters

can be written as

$$\mathcal{E}_{\rm ns}(k) = D(k)\frac{\Omega\mathcal{E}_{\rm n}(k) + \Omega_{\rm n}\mathcal{E}_{\rm s}(k)}{\Omega_{\rm ns}},$$
$$\Omega_{\rm n} = \Omega\rho_{\rm s}/\rho_{\rm n}, \quad \Omega_{\rm ns} = \Omega + \Omega_{\rm n}. \tag{26}$$

Here, $D(k) = \arctan[\zeta(k)]/\zeta(k)$ is the dimensionless "decoupling function," defined via the dimensionless "decoupling parameter" $\zeta(k) = kU_{\rm ns}/\Omega_{\rm ns}$. It describes the decoupling of the normal and superfluid velocity fluctuations, caused by counterflow [31].

In the steady-state case, Eqs. (24)–(26) take the form

$$\frac{5}{8}\frac{d}{dk}\,k^{5/2}\mathcal{E}_{\rm s,n}^{3/2}(k) = \Omega_{\rm s,n}\left\{\frac{\Omega\,\mathcal{E}_{\rm s}(k) + \Omega_{\rm n}\,\mathcal{E}_{\rm n}(k)}{\Omega_{\rm ns}}D(k) - \mathcal{E}_{\rm s,n}\right\}, \tag{27}$$

that will be referred to as "*differential model for the superfluid energy spectra*."

B. Energy spectra in "symmetric" counterflow turbulence with $\rho_{\rm n} = \rho_{\rm s}$

The system of ordinary differential equations (26) can be solved numerically for any temperature. This task will be done elsewhere. Here, we consider a particular temperature $T \simeq 1.95$ K, for which $\rho_{\rm n} \simeq \rho_{\rm s}$. In this case, we expect $\mathcal{E}_{\rm s}(k) = \mathcal{E}_{\rm n}(k) \equiv \mathcal{E}$ and Eqs. (26) become an ordinary differential equation for $\mathcal{E}(k)$:

$$\frac{5}{8}\frac{d}{dk}\,k^{5/2}\mathcal{E}^{3/2}(k) = \Omega\,\mathcal{E}(k)\,[D(k) - 1], \tag{28}$$

which can be solved analytically.

To this end, we nondimensionalize them by introducing a dimensionless wave number $q = k/k_0$ with $k_0 \simeq \pi/\Delta$ and the outer scale of turbulence Δ is defined such that Eqs. (26) are valid for $q > 1$. We introduce also a dimensionless parameter

$$\zeta_q = q/q_\times, \quad q_\times = 2\,\Omega/(k_0 V_{\rm ns}), \tag{29a}$$

and a new dimensionless function

$$\Psi(q) \equiv \frac{15\,k_0^{3/2}}{8\,\Omega}\sqrt{q^{5/3}\mathcal{E}(q\,k_0)}, \tag{29b}$$

$$\mathcal{E}(k) = \left[\frac{8\Psi(k/k_0)}{15}\right]^2\frac{\Omega^2}{k_0^{4/3}k^{5/3}}. \tag{29c}$$

Then, Eq. (28) takes a simple form

$$q^{5/3}\frac{d\,\Psi(q)}{dq} = D(q/q_\times) - 1, \tag{30}$$

which can be solved analytically with the boundary condition at $q = 1$ (i.e., $k = k_0$):

$$\Psi(1) = \Psi_0 = \frac{8\Omega}{15\sqrt{k_0^3\mathcal{E}_0}}, \tag{31a}$$

$$\Psi(q) = \Psi_0 + \frac{1}{q_\times^{2/3}}\left[I\left(\frac{1}{q_\times}\right) - I\left(\frac{q}{q_\times}\right)\right], \tag{31b}$$

$$I(z) = \int_0^z \frac{1 - D(y)}{y^{5/3}}dy. \tag{31c}$$

Using now Eqs. (29c) and (31) one gets

$$\mathcal{E}(k) = \mathcal{E}_0\left\{1 + A\left[I\left(\frac{k}{k_\times}\right) - I\left(\frac{k_0}{k_\times}\right)\right]\right\}^2\left(\frac{k_0}{k}\right)^{5/3}, \tag{32a}$$

$$A = \frac{8\,\Omega\,k_0^{2/3}}{15\,k_\times^{2/3}\sqrt{k_0^3\mathcal{E}_0}}, \quad k_\times = \frac{2\Omega_{\rm ns}}{U_{\rm ns}}. \tag{32b}$$

Integral (31c) can be found analytically:

$$I(z) = \frac{\sqrt{3}\pi}{5} + \frac{3}{20}\left\{-\frac{4}{z^{2/3}} - 2\sqrt{3}\arctan[\sqrt{3} - 2z^{1/3}]\right.$$
$$- 2\sqrt{3}\arctan[\sqrt{3} + 2z^{1/3}] + \frac{4\arctan[z]}{z^{5/3}}$$
$$\left. + \ln\left[1 - \frac{3z^{2/3}}{(1 + z^{2/3})^2}\right]\right\}. \tag{32c}$$

It has the following asymptotics:

$$I(z) = \frac{z^{4/3}}{4}\left(1 - \frac{6z^2}{25}\right) \quad \text{for} \quad z \ll 1, \tag{33a}$$

$$I(z) = \frac{\sqrt{3}\,\pi}{5} - \frac{3}{2z^{2/3}} \quad \text{for} \quad z \gg 1. \tag{33b}$$

A simple analytical expression

$$I(z) \simeq \frac{z^{4/3}}{4 + 0.7z^2} \tag{33c}$$

approximates the exact Eq. (32c), with the relative accuracy within 3% in the $z < 2$ region, while the expression

$$I(z) = \frac{\sqrt{3}\,\pi}{5} - \frac{3}{2z^{2/3}} + \frac{\pi}{4z^{5/3}} \tag{33d}$$

works well for $z > 2$.

Notice that for $k_0 < k \ll k_\times$, the energy spectrum (32) deviates down from the K41 $\frac{5}{3}$ spectrum:

$$\mathcal{E}(k) \simeq \mathcal{E}_0\left\{1 + \frac{A}{4\,k_\times^{4/3}}\left[k_0^{4/3} - k^{4/3}\right]\right\}^2\left(\frac{k_0}{k}\right)^{5/3}. \tag{34}$$

The spectrum for $k \gg k_\times$ crucially depends on the value of A. There exists a critical value

$$A_{\rm cr} = 1/I(\infty) = 5/(\pi\sqrt{3}) \approx 0.92. \tag{35}$$

For $A < A_{\rm cr}$ the system asymptotically tends to K41 spectrum

$$\mathcal{E}(k) \simeq \mathcal{E}_0\left\{1 - \frac{A}{A_{\rm cr}}\right\}^2\left(\frac{k_0}{k}\right)^{5/3}, \tag{36}$$

but with the energy flux $\varepsilon_\infty = \varepsilon_0(1 - A/A_{\rm cr})^3$, smaller than the energy input rate ε_0. The difference $(\varepsilon_0 - \varepsilon_\infty)$ is dissipated by mutual friction. This is similar to the subcritical LNV spectrum (6) of ^{3}He turbulence with resting normal-fluid component.

For $A > A_{\rm cr}$, $\mathcal{E}(k) = 0$ for large k. In the differential approximation used here, the spectrum $\mathcal{E}(k)$ sharply terminates at some finite k_*, in the same manner as the supercritical LNV ^{3}He spectrum (7). The cutoff wave number k_* may be found

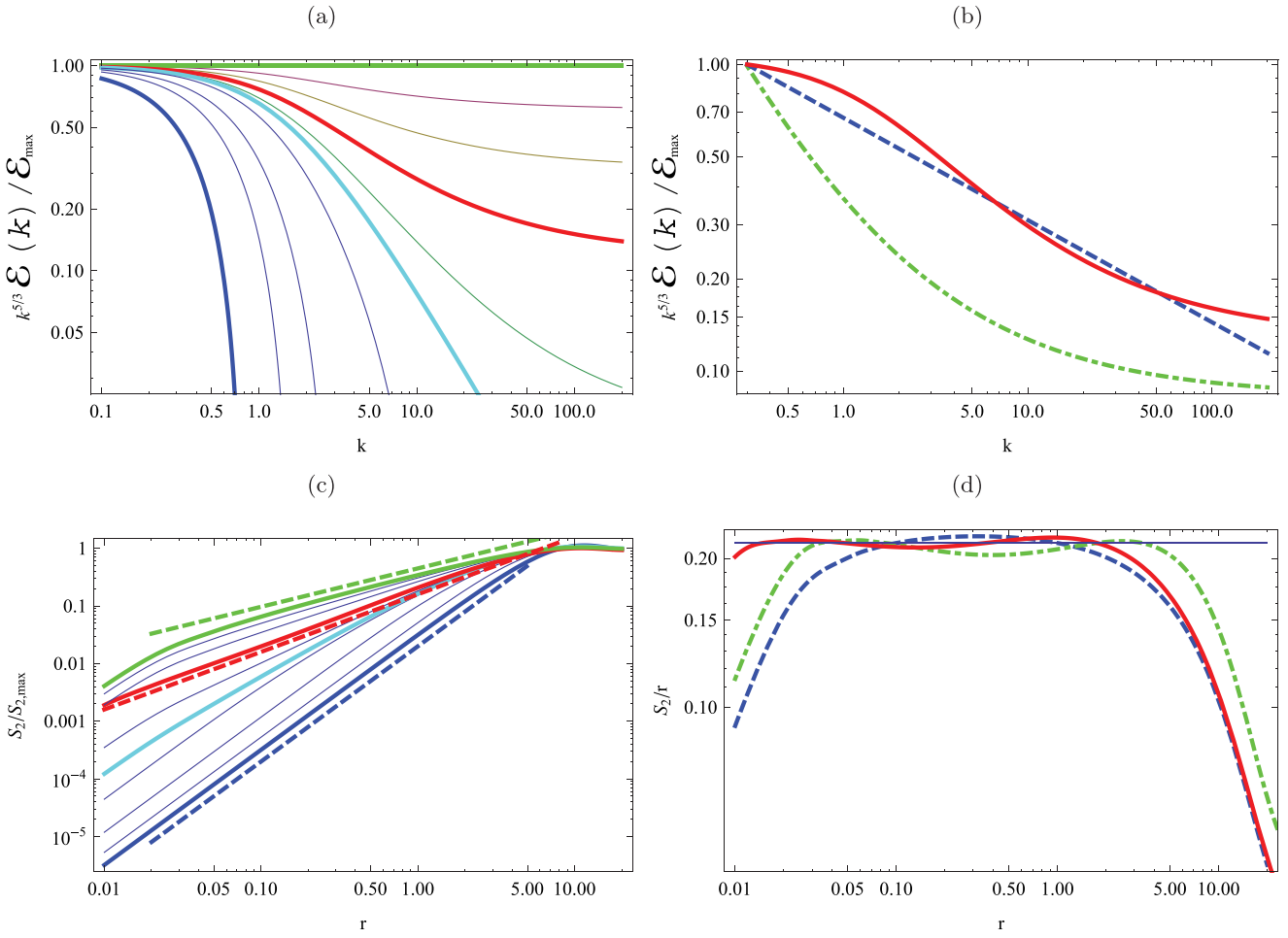

FIG. 11. (a) Log-log plots of compensated normalized energy spectra $k^{5/3}\mathcal{E}(k)/\mathcal{E}_{\max}$ for $k_0 = 0$ and with different values of A, starting with $A = 0$ (upper green line), through $A = 0.2,\ 0.4,\ 0.6$ (red thick line), $0.8, 0.92$ (thick cyan line, critical value), $1,\ 1.5,\ 2.0\,3.0$ and last line, $A = 6$. (b) Log-log plots of compensated normalized energy spectrum $k^{5/3}\mathcal{E}(k)/\mathcal{E}_{\max}$ for $k_0 = 0.3k_\times$ with $A = 0.6$ (solid red line), $1/k^2$ (after compensation by $k^{5/3}$) (blue dashed line), and LNV subcritical spectrum $k^{-3}[1 + (k/k_*)^{2/3}]^2$ with $k_* = 1.15k_\times$ (green dashed-dotted line). (c) Log-log plots of the second-order structure functions $S_2(r)$ (normalized by their large-r limit), computed with Eq. (39a) and with the same values of A (and the same color code) as in (a). The thick dashed straight lines indicate scaling laws: upper green line $\propto r^{2/3}$, middle red line $\propto r$, and lower blue line $\propto r^2$. (d) The normalized compensated by $1/r$ structure functions $S_2(r)$, calculated using the spectra shown in (b) (with the same color code).

from the equation

$$1 = A[I(\zeta_{k_*}) - I(\zeta_0)] \approx A\, I(\zeta_{k_*}). \tag{37}$$

When $A \to A_{\rm cr}$, $k_* \to \infty$ and $\mathcal{E}(k) \propto k^{-3}$ at large k, exactly like in the critical LNV ^{3}He spectrum (5).

The energy spectra (32) for different values of A in the range $0 \leqslant A \leqslant 6$, that includes the critical value $A_{\rm cr} \simeq 0.92$, are shown in Fig. 11(a). We see that increase in the mutual friction force, characterized in Eq. (32) by the dimensionless parameter A, suppresses the energy spectra from the Kolmogorov-41 behavior $\mathcal{E}(k) \propto k^{-5/3}$ (for $A = 0$) towards the critical spectrum $\mathcal{E}(k) \propto k^{-3}$ at $A = A_{\rm cr} \simeq 1$. Further increase in A localizes energy spectra in the k space, as shown in Fig. 4(b). There is clear qualitative similarity of the energy spectra in counterflow turbulence with the LNV spectra. This allowed us to use the LNV spectra in Sec. III C for the analysis of the delay function $F_{\rm del}(t)$ in our improved model of the VLD decay.

C. Velocity structure functions in "symmetric" counterflow turbulence

Recent visualization experiment in counterflow [39] reported that transversal velocity structure function $S_{2,\perp}(r) \propto r$ in an interval about one decade, adjacent to the outer scale of turbulence. To see how these observations may be rationalized using our model, we consider the second-order velocity functions, defined as follows:

$$S_2(\boldsymbol{r}) = \langle |\boldsymbol{u}(\boldsymbol{r}) - \boldsymbol{u}(0)|^2 \rangle, \tag{38a}$$

$$S_{2,\perp}(\boldsymbol{r}) = \langle [u_\perp(\boldsymbol{r}) - u_\perp(0)]^2 \rangle, \tag{38b}$$

$$S_{2,\parallel}(\boldsymbol{r}) = \langle [u_\parallel(\boldsymbol{r}) - u_\parallel(0)|^2 \rangle. \tag{38c}$$

Here, $u_\perp$ and $u_\parallel$ are projections of the turbulent velocity $\boldsymbol{u}$ on directions orthogonal and parallel to the separation $\boldsymbol{r}$. In isotropic turbulence, assumed above in the analytical model of the spectra, all structure functions depend only on $r = |\boldsymbol{r}|$ and all are proportional to each other. Up to a numerical factor of the order unity, they may be expressed via 1D energy spectrum $\mathcal{E}(k)$ as follows:

$$S_2(r) \simeq \int_0^\infty \mathcal{E}(k)[1 - \sin(kr)/(kr)]\, dk. \tag{39a}$$

With the K41 spectrum $\mathcal{E}_{\text{K41}}(k) = \mathcal{E}_0(k_0/k)^{5/3}$ [Eq. (32) with $A = 0$], it gives the classical result

$$S_2(r) \simeq 1.2V_{\text{T}}^2(k_0 r)^{2/3}, \quad V_{\text{T}} \equiv \sqrt{k_0\, \mathcal{E}_0}, \tag{39b}$$

shown by the upper green dashed straight line in Fig. 11(c). Next, we account for the fact that in reality the available range of k is limited: $k_{\min} < k < k_{\max}$. The value of $k_{\min} \sim \pi/\Delta$ is determined by the outer scale of turbulence. For quantum turbulence in the superfluid component, $k_{\max} \simeq \pi/\ell$. In the Florida experiments [39], our estimates show that $k_{\min} \simeq 0.3k_\times$ and $k_{\max} \simeq 200k_\times$. Replacing limits in the integral (39a) by these values, we compute again $S_2(r)$ with the K41 spectrum [see upper green solid line in Fig. 11(c)]. We observe the same scaling behavior $S_2(r) \propto r^{2/3}$ in the interval of about two decades (from $r \simeq 0.05$ to 5). For nonzero values of A, the log-log plots of $S_2(r)$ versus r can be considered as approximately straight lines with the slope that increases with A. In particular, for $A = 0.6$ $S_2(r)$, shown in Fig. 11(c) by solid red line, it is practically indistinguishable from the straight line with the slope $+1$ (shown by dashed red line) in the interval $0.02 < r < 2$. This means that, for $A = 0.6$, $S_2(r) \propto r$ with high accuracy in the interval of two decades. To see this better, in Fig. 11(d) we present the plot of $S_2(r)$ compensated by $1/r$. The solid red line in Fig. 11(d) lays indeed very close to the black thin horizontal line.

Notice that the energy spectrum for $A = 0.6$, used to find $S_2(r)$ [red solid line in Fig. 11(b)], is essentially different from the scale-invariant spectrum $\mathcal{E}(k) \propto k^{-2}$, shown in Fig. 11(b) by the dashed blue line. Using spectrum $\mathcal{E}(k) \propto k^{-2}$, we computed $S_2(r)$ again, with the result shown in Fig. 11(d) by the dashed blue line. Unexpectedly, this result demonstrates scale-invariant behavior $S_2(r) \propto r$ on a shorter range. We also computed $S_2(r)$ using subcritical LNV spectrum (6), with the critical wave number $k_{\text{cr}} = 1.15k_0$. This spectrum, shown in Fig. 11(b) by the green dashed-dotted line, is very different from the $1/k^2$ behavior (blue dashed line). Nevertheless, the resulting structure function $S_2(r)$ [green dashed-dotted line in Fig. 11(d)] again demonstrates the scale-invariant behavior of $S_2(r) \propto r$ over more than two decades.

We conclude that very different energy spectra, including the spectrum (32) with $A \simeq 0.6$, found here, can result in the reported in Ref. [39] $S_2(r) \propto r$ with somewhat smaller extent of the scaling behavior, of about one decade. This means that our analytical model does not contradict the observation [39]. Nevertheless, at this stage we are not in the position to claim that the model explains the observed simple behavior $S_2(r) \propto r$. We will return to this point in conclusive Sec. V.

Here, we notice only that, as the parameter A increases, the energy spectra become more and more localized at small k, as seen in Fig. 11(a), while the apparent slope of the corresponding structure functions increases, tending to 2. This is clearly seen in Fig. 11(c). The $S_2(r)$ for the largest $A = 6$ is shown by solid blue line in comparison with the scaling function r^2, shown by the blue dashed line. The reason for such a behavior is simple: for large A, the energy spectrum terminates at small k and for scales smaller than $1/k$, the velocity field becomes smooth and differentiable. Thus, the velocity field can be expanded in the Taylor series, the velocity difference across the separation r is proportional to r, and the structure function is proportional to r^2.

D. Approximations of the simple analytical model

It should be stressed that in our approach we adopted some uncontrolled approximations and simplifications, widely used in the studies of classical hydrodynamic turbulence. Among them are celebrated hypotheses, suggested by Kolmogorov in 1941, concerning the small-scale turbulent statistics:

(1) universality (independence of the energy pumping);
(2) isotropy;
(3) locality of energy transfer over scales.

These hypotheses have been justified in numerous experiments, numerical and analytical studies of developed turbulence of classical fluids, mechanically driven at large scales. However, very little is known about turbulent statistics in the case of thermally driven quantum counterflow turbulence.

We can quite easily justify the first hypothesis of the universality, for instance, in the wide and long enough channels with reasonably well-controlled surface of the wall. The second assumption is the isotropy hypothesis. It is known from numerical simulations of (mainly space homogeneous) counterflow turbulence that the anisotropy of the quantized vortex tangle is rather small (about 10%) (see, e.g., [34,36,41,42]. However, very little is known about anisotropy of the velocity fluctuations on scales R above the intervortex distance ℓ. Without this knowledge and having clear understanding that the assumption of isotropy on scales $R > \ell$ may be questionable, we nevertheless assume isotropy of turbulence statistics from the very beginning. This simplifying assumption allows us to formulate a simple analytical model in terms of one-dimensional energy spectrum $\mathcal{E}(k)$, which is an angular average of the full (and possibly anisotropic) three-dimensional energy spectrum.

The third assumption is the locality of the energy transfer, which is built-in in the algebraic closure (25b), used in our approach. This assumption may also be justified, taking into account that the nonlinear terms in the two-fluid equations of motion for the normal and superfluid velocity components are the same as in the Navier-Stokes equation, if the resulting energy spectrum is not very different from the classical $\frac{5}{3}$ scaling for the classical fluid. The detailed analysis of the problem of locality in classical turbulence with the scale-invariant scaling $\mathcal{E}(k) \propto k^{-x}$ shows [43,44] that in the "window of locality" $1 < x < 3$ the energy transfer is really local. For our case, this means that for the subcritical spectra {with $A < 1$, when the the local slope $x(k) = d\ln[\mathcal{E}(k)]/d\ln k$ is within the window of locality}, this assumption is reasonable. We also hope that the strong version of the locality assumption, the algebraic closure (25b), leads to qualitatively correct energy spectra.

The situation with the supercritical spectra is less simple. Definitely, the consequence of Eqs. (32) and (7) that $\mathcal{E}(k) = 0$ for $k > k_*$ is an artifact of the algebraic closure. We think that for large k, the supercritical energy spectra will instead decay very fast with k, presumably $\propto k^{-y}$ with $y > 3$, as a result of the direct (nonlocal) energy transfer to the k region from the intermediate region of scales about $k_{\rm int}$, where the local slope $x(k_{\rm int}) \simeq 5$.

Last but not least, an additional restriction of our approach is full ignorance of possible long-living coherent structures at scales $\gtrsim \ell$ that may contribute to the statistics of quantum turbulence with counterflow. There is a great deal of speculation in the studies of classical space-homogeneous hydrodynamic turbulence, but, nevertheless, the question of their statistical relevance is still open. Moreover, the well-justified multifractal models of classical turbulence (see, e.g., [27]) describe in many details the statistics of classical turbulence without any direct reference to coherent structures. Coherent structures in quantum turbulence can be characterized simply as "terra incognita."

In such a situation, much more experimental, numerical, and analytical work is required to formulate a theory of quantum turbulence which will account for the interplay of coexisting classical and quantum forms of superfluid turbulent energy in all relevant details. Nevertheless, we consider our experimental findings and simple analytical models of steady-state and decaying quantum turbulence as a natural and perhaps even required step in a long way toward desired level of understanding and description of the basic physical mechanisms that govern quantum turbulence.

V. SUMMARY

Being motivated by the challenge to understand the quantum turbulence occurring in superfluid ^{4}He, at finite $T \gtrsim 1$ K where it displays the two-fluid behavior, we report this complementary experimental, numerical, and theoretical treatise of turbulent coflow, counterflow, and pure superflow of superfluid ^{4}He in a channel. The level of agreement between the experimental observations and the analytical predictions for the time evolution of the vortex-line density in decaying turbulence, demonstrated in this paper, allows us to conclude that the developed basic and improved models adequately reflect the underlying physical processes responsible for the decay of quantum turbulence, originating from various types of steady superfluid ^{4}He flows (coflow, counterflow, pure superflow), including (i) the interplay of classical and quantum processes, resulting in two decay laws of VLD; (ii) the partial decoupling of the normal and superfluid velocity fields in pure superflow and counterflow turbulence, predicted in Ref. [31]; (iii) the resulting suppression of energy spectra in these flows leading to the time delay in the energy flux from classical to quantum length scales of turbulence in superfluid ^{4}He.

Being inspired by these findings, we made the first step towards the theory of steady-state, space homogeneous turbulence of counterflowing superfluid ^{4}He. The suggested by us simple analytical theory results in the energy spectra $\mathcal{E}(k, A)$ given by Eq. (32) and shown in Fig. 11(a). These spectra depend on the dimensionless parameter A, that describes the intensity of the mutual friction, responsible for the coupling of the normal and superfluid velocity, relative to the counterflow velocity, responsible for their decoupling. For the particular value $A \simeq 0.6$, the energy spectrum $\mathcal{E}(k,0.6)$, shown in Fig. 11(b) is close to $1/k^2$ scaling and results in the second-order structure function $S_2(r) \propto r$ over the interval of about two decades, in agreement with the observations reported in Ref. [39].

ACKNOWLEDGMENTS

We thank W. F. Vinen and W. Guo for interesting discussions. This work is supported by the Czech Science Foundation under Project No. GAČR 203/14/02005S and by the European Community Framework Programme 7, EuHIT (European High-performance Infrastructures in Turbulence) Grant Agreement No. 312778.

APPENDIX A: SABRA-SHELL MODEL OF QUANTUM TURBULENCE

A detailed study of the decay of large-scale turbulence has been done in the framework of the so-called Sabra-shell model of quantum turbulence [29,33,38]:

$$\left[\frac{d}{dt} + \nu_{\rm n} k_m^2\right] u_m^{\rm n} = {\rm NL}\left[u_m^{\rm n}\right] + F_m^{\rm n}, \tag{A1a}$$

$$\left[\frac{d}{dt} + \nu_{\rm s} k_m^2\right] u_m^{\rm s} = {\rm NL}\left[u_m^{\rm s}\right] - F_m^{\rm s}, \tag{A1b}$$

$$\begin{aligned} {\rm NL}[u_m] = i(&a k_{m+1} u_{m+2} u_{m+1}^* + b k_m u_{m+1} u_{m-1}^* \\ &- c k_{m-1} u_{m-1} u_{m-2}), \end{aligned} \tag{A1c}$$

$$F_m^{\rm s} = \Omega\left(u_m^{\rm s} - u_m^{\rm n}\right),$$

$$F_m^{\rm n} = \Omega_{\rm n}\left(u_m^{\rm s} - u_m^{\rm n}\right). \tag{A1d}$$

These equations represent a simplified version of the coarse-grained, two-fluid, gradually damped Hall-Vinen-Bekarevich-Khalatnikov (HVBK) equations in the $\boldsymbol{k}$ representation. They mimic the statistical behavior of $\boldsymbol{k}$-Fourier components of the turbulent superfluid and normal velocity fields in the entire shell of wave vectors $k_m < k < k_{m+1}$ by complex shell velocity $u_m^{\rm n,s}$. The shell wave numbers are chosen as a geometric progression $k_m = k_0 \lambda^m$, where $m = 1,2,\ldots M$ are the shell indexes, and we have used the shell-spacing parameter $\lambda = 2$, $k_0 = \frac{1}{16}$, and $M = 28$ shells.

Similarly to the HVBK (and the Navier-Stokes or Euler equation), the NL$[u_m]$ term in Eq. (A1c) is quadratic in velocities, proportional to k, and conserves (in the forceless, inviscid limit) the kinetic energy $E = \frac{1}{2}\sum_m |u_m|^2$, provided that $a + b + c = 0$. We used here the Sabra version [45] of NL$[u_m]$ with the traditional (and physically motivated) choice $b = c = -a/2$, which describes important features of superfluid turbulence including intermittency corrections [29].

In Eq. (A1a), $\nu_{\rm n} = \mu/\rho_{\rm n}$ is the kinematic viscosity of the normal component, i.e., its dynamical viscosity μ, normalized by the normal fluid density. The effective superfluid viscosity $\nu_{\rm s}$ describes the energy sink in superfluids, e.g., due to the vortex reconnections. For more details of the origin and role of $\nu_{\rm s}$, see Refs. [2,29]. The mutual friction term $F_m^{\rm n,s}$ is given by Eq. (A1d).

As a first step in our study of the large-scale turbulence decay we can simplify the procedure further, using the fact that the turnover time in our situations is longer than the coupling time $1/\Omega_{ns}$ given by Eq. (26). Therefore, the first stage of the decay, during which the normal and superfluid velocities become coupled, is short with respect to the time required for the developing of the Richardson-Kolmogorov cascade. Skipping this stage, we can assume that the velocities are fully coupled. In this case, Eqs. (A1) turn into one Sabra equation for $u_m = u_m^s = u_m^n$:

$$\left[\frac{d}{dt} + \nu k_m^2\right] u_m = \mathrm{NL}[u_m]\,, \tag{A2}$$

with $\nu = (\mu + \nu_s\rho_s)/\rho$.

The equations (A2) were solved using the adaptive time step fourth-order Runge-Kutta with exponential time differencing [46]. For more details, see Refs. [33,38]. The evolution of the system was followed for about $10^3\tau_\Delta$. In all cases, we perform 10^4 simulations with the same initial total energy, but different, randomly distributed phases of initial shell velocities and perform ensemble averaging over initial conditions.

APPENDIX B: SOME DEFINITIONS AND KNOWN RELATIONSHIPS

To define the one-dimensional energy spectra $\mathcal{E}_n(k)$, $\mathcal{E}_s(k)$ and cross correlation $\mathcal{E}_{ns}(k)$ we need to recall some definitions and relationships, that are well known in statistical physics. The first is the set of Fourier transforms in the following normalization:

$$\boldsymbol{u}'_{n,s}(\boldsymbol{r},t) \equiv \int \frac{d\boldsymbol{k}}{(2\pi)^3}\, \boldsymbol{v}_{n,s}(\boldsymbol{k},t)\exp(i\boldsymbol{k}\cdot\boldsymbol{r}), \tag{B1a}$$

$$\boldsymbol{v}_{n,s}(\boldsymbol{k},t) \equiv \int \frac{d\omega}{2\pi}\, \widetilde{\boldsymbol{v}}_{n,s}(\boldsymbol{k},\omega)\exp(-i\omega t), \tag{B1b}$$

$$\widetilde{\boldsymbol{v}}_{n,s}(\boldsymbol{k},\omega) = \int d\boldsymbol{r}\, dt\, \boldsymbol{u}'_{n,s}(\boldsymbol{r},t)\exp[i(\omega t - \boldsymbol{k}\cdot\boldsymbol{r})]. \tag{B1c}$$

The same normalization is used for other objects of interest.

Next, we define the simultaneous correlations and cross correlations in $\boldsymbol{k}$ representation [proportional to $\delta(\boldsymbol{k}-\boldsymbol{k}')$ due to homogeneity]:

$$\langle \boldsymbol{v}_n(\boldsymbol{k},t)\cdot\boldsymbol{v}_n^*(\boldsymbol{k}',t)\rangle = (2\pi)^3 E_{nn}(\boldsymbol{k})\,\delta(\boldsymbol{k}-\boldsymbol{k}'), \tag{B2a}$$

$$\langle \boldsymbol{v}_s(\boldsymbol{k},t)\cdot\boldsymbol{v}_s^*(\boldsymbol{k}',t)\rangle = (2\pi)^3 E_{ss}(\boldsymbol{k})\,\delta(\boldsymbol{k}-\boldsymbol{k}'), \tag{B2b}$$

$$\langle \boldsymbol{v}_n(\boldsymbol{k},t)\cdot\boldsymbol{v}_s^*(\boldsymbol{k}',t)\rangle = (2\pi)^3 E_{ns}(\boldsymbol{k})\,\delta(\boldsymbol{k}-\boldsymbol{k}'). \tag{B2c}$$

We also need to define cross correlations $\langle\widetilde{\boldsymbol{v}}_n\cdot\widetilde{\boldsymbol{v}}_s^*\rangle$ in $(\boldsymbol{k},\omega)$ representation:

$$\langle \widetilde{\boldsymbol{v}}_n(\boldsymbol{k},\omega)\cdot\widetilde{\boldsymbol{v}}_s^*(\boldsymbol{k}',\omega')\rangle = (2\pi)^4 \widetilde{E}_{ns}(\boldsymbol{k},\omega)\,\delta(\boldsymbol{k}-\boldsymbol{k}')\,\delta(\omega-\omega'). \tag{B3a}$$

This object is related to the simultaneous $\langle \boldsymbol{v}_n\cdot\boldsymbol{v}_s^*\rangle$ cross correlation (B2c) via the frequency integral

$$\langle \boldsymbol{v}_n(\boldsymbol{k},t)\cdot\boldsymbol{v}_s^*(\boldsymbol{k}',t)\rangle = \int d\omega\, \widetilde{E}_{ns}(\boldsymbol{k},\omega). \tag{B3b}$$

Here and below, "tilde" marks the objects defined in $(\boldsymbol{k},\omega)$ representation.

It is known also that the $\boldsymbol{k}$ integration of the correlations (B2) produces their one-point second moment:

$$\int \frac{d\boldsymbol{k}}{(2\pi)^3} E_{nn}(\boldsymbol{k},t) = \langle|\boldsymbol{u}_n(\boldsymbol{r},t)|^2\rangle, \tag{B4a}$$

$$\int \frac{d\boldsymbol{k}}{(2\pi)^3} E_{ss}(\boldsymbol{k},t) = \langle|\boldsymbol{u}_s(\boldsymbol{r},t)|^2\rangle, \tag{B4b}$$

$$\int \frac{d\boldsymbol{k}}{(2\pi)^3} E_{ns}(\boldsymbol{k},t) = \langle\boldsymbol{u}_n(\boldsymbol{r},t)\cdot\boldsymbol{u}_s(\boldsymbol{r},t)\rangle. \tag{B4c}$$

In the isotropic case, each of the three correlations $E_{...}(\boldsymbol{k})$ is independent of the direction of $\boldsymbol{k}$: $E_{...}(\boldsymbol{k}) = E_{...}(k)$ and $\int\ldots d\boldsymbol{k} = 4\pi\int\ldots k^2\,dk$. This allows the introduction of the one-dimensional energy spectra $\mathcal{E}_s$, $\mathcal{E}_n$ and the cross correlation $\mathcal{E}_{ns}$ as follows:

$$\mathcal{E}_n(k,t) = \frac{k^2}{2\pi^2}E_{nn}(k,t), \quad \mathcal{E}_s(k,t) = \frac{k^2}{2\pi^2}E_{ss}(k,t),$$
$$\mathcal{E}_{ns}(k) \equiv \frac{k^2}{2\pi^2}E_{ns}(k,t). \tag{B5}$$

[1] C. F. Barenghi, L. Skrbek, and K. R. Sreenivasan, Proc. Natl. Acad. Sci. U. S. A. **111**, 4647 (2014).

[2] W. F. Vinen and J. J. Niemela, J. Low Temp. Phys. **128**, 167 (2002).

[3] L. Skrbek and K. R. Sreenivasan, Phys. Fluids **24**, 011301 (2012).

[4] R. J. Donnelly, *Quantized Vortices in Hellium II* (Cambridge University Press, Cambridge, 1991).

[5] *Quantized Vortex Dynamics and Superfluid Turbulence*, edited by C. F. Barenghi, R. J. Donnelly, and W. F. Vinen, Lecture Notes in Physics 571 (Springer, Berlin, 2001).

[6] L. Skrbek and K. R. Sreenivasan, in *Ten Chapters in Turbulence*, edited by P. A. Davidson, Y. Kaneda, and K. R. Sreenivasan (Cambridge University Press, Cambridge, 2013), pp. 405–437.

[7] C. F. Barenghi, V. S. L'vov, and P.-E. Roche, Proc. Natl. Acad. Sci. U. S. A. **111**, 4683 (2014).

[8] P. L. Walstrom, J. G. Weisend, J. R. Maddocks, and S. W. Van Sciver, Cryogenics **28**, 101 (1988).

[9] S. Babuin, E. Varga, and L. Skrbek, J. Low Temp. Phys. **175**, 324 (2014).

[10] S. Babuin, E. Varga, L. Skrbek, E. Leveque, and P.-E. Roche, Europhys. Lett. **106**, 24006 (2014).

[11] E. Varga, S. Babuin, and L. Skrbek, Phys. Fluids **27**, 065101 (2015).

[12] M. R. Smith, R. J. Donnelly, N. Goldenfeld, and W. F. Vinen, Phys. Rev. Lett. **71**, 2583 (1993).

[13] S. R. Stalp, L. Skrbek, and R. J. Donnelly, Phys. Rev. Lett. **82**, 4831 (1999).

[14] H. E. Hall and W. F. Vinen, Proc. R. Soc. A **238**, 204 (1956).

[15] K. W. Schwarz and J. R. Rozen, Phys. Rev. Lett. **66**, 1898 (1991).
[16] H. Tennekes and J. L. Lumley, *A First Course in Turbulence* (The MIT Press, Cambridge, MA, 1994).
[17] H. Schlichting and K. Gersten, *Boundary-Layer Theory*, (Springer, Berlin, 2000).
[18] M. L. Baehr and J. T. Tough, Phys. Rev. Lett. **53**, 1669 (1984).
[19] S. S. Courts and J. T. Tough, Phys. Rev. B **38**, 74 (1988).
[20] W. F. Vinen, Proc. R. Soc. A **240**, 114 (1957); **240**, 128 (1957); **243**, 400 (1958); **242**, 493 (1957).
[21] S. Babuin, E. Varga, W. F. Vinen, and L. Skrbek, Phys. Rev. B **92**, 184503 (2015).
[22] J. Gao, W. Guo, V. S. L'vov, A. Pomyalov, L. Skrbek, E. Varga, and W. F. Vinen, JETP Lett. **103**, 648 (2016).
[23] S. Babuin, M. Stammeier, E. Varga, M. Rotter, and L. Skrbek, Phys. Rev. B **86**, 134515 (2012).
[24] L. Skrbek, A. V. Gordeev, and F. Soukup, Phys. Rev. E **67**, 047302 (2003).
[25] A. V. Gordeev, T. V. Chagovets, F. Soukup, and L. Skrbek, J. Low Temp. Phys. **138**, 549 (2005).
[26] R. J. Donnelly and C. F. Barenghi, J. Phys. Chem. Ref. Data **27**, 1217 (1998).
[27] U. Frisch, *Turbulence: The Legacy of A. N. Kolmogorov*, (Cambridge University Press, Cambridge, 1995).
[28] V. S. L'vov, S. V. Nazarenko, and L. Skrbek, J. Low Temp. Phys. **145**, 125 (2006).
[29] L. Boue, V. S. L'vov, Y. Nagar, S. V. Nazarenko, A. Pomyalov, and I. Procaccia, Phys. Rev. B **91**, 144501 (2015).
[30] C. Connaughton and S. Nazarenko, Phys. Rev. Lett. **92**, 044501 (2004).
[31] D. Khomenko, V. S. L'vov, A. Pomyalov, and I. Procaccia, Phys. Rev. B **93**, 014516 (2016).
[32] V. S. L'vov, S. V. Nazarenko, and G. E. Volovik, JETP Lett. **80**, 479 (2004).
[33] L. Boue, V. S. L'vov, A. Pomyalov, and I. Procaccia, Phys. Rev. B **85**, 104502 (2012).
[34] K. W. Schwarz, Phys. Rev. B **38**, 2398 (1988).
[35] K. W. Schwarz, Phys. Rev. B **31**, 5782 (1985).
[36] L. Kondaurova, V. S. L'vov, A. Pomyalov, and I. Procaccia, Phys. Rev. B **89**, 014502 (2014).
[37] D. Khomenko, V. S. L'vov, A. Pomyalov, and I. Procaccia, Phys. Rev. B **93**, 134504 (2016)
[38] L. Boué, V. S. L'vov, A. Pomyalov, and I. Procaccia, Phys. Rev. Lett. **110**, 014502 (2013).
[39] A. Marakov, J. Gao, W. Guo, S. W. Van Sciver, G. G. Ihas, D. N. McKinsey, and W. F. Vinen, Phys. Rev. B **91**, 094503 (2015).
[40] L. Kovasznay, J. Aeronaut. Sci. **15**, 745 (1947).
[41] R. T. Wang, C. E. Swanson, and R. J. Donnelly, Phys. Rev. B **36**, 5240 (1987).
[42] H. Adachi, S. Fujiyama, and M. Tsubota, Phys. Rev. B **81**, 104511 (2010).
[43] V. S. L'vov and G. E. Falkovich, Phys. Rev. A **46**, 4762 (1992).
[44] V. S. L'vov and I. Procaccia. Phys. Rev. E **52**, 3840 (1995)
[45] V. S. L'vov, E. Podivilov, A. Pomyalov, I. Procaccia, and D. Vandembroucq, Phys. Rev. E **58**, 1811 (1998).
[46] S. M. Cox and P. C. Matthews, J. Comput. Phys. **176**, 430 (2002).